Experimental calibration of an active space telescope with flexure joints

Thibault Gayral, David Daney

RESEARCH REPORT

N° 8096

October 2012

Project-Team Coprin

ISSN 0249-6399 ISRN INRIA/RR--8096--FR+ENG

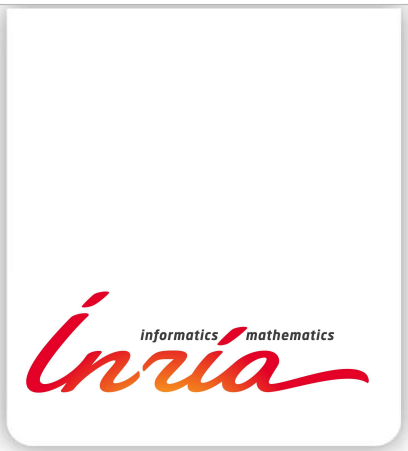

Experimental calibration of an active space telescope with flexure joints

Thibault Gayral, David Daney

Project-Team Coprin

Research Report n° 8096 — version 2* — initial version October 2012 — revised version October 2012 — 40 pages

Abstract: In order to reach a micrometer accuracy, a suitable model of a space telescope needs to be developed and validated through calibration. Since high velocity is not required in such an application, the dynamic effects can be neglected and only geometric and/or static calibration has to be considered. Moreover, measurements for calibration are performed in a clean room under controlled pressure, temperature and humidity conditions to minimize the influence of the non-geometric errors. Thus, two possible static inaccuracy sources are identified and modelled: one from the deformation of the mobile platform and the other resulting from the behaviour of the flexure joints. Their influences on the final accuracy of the telescope are compared through results of calibration using an accurate measurement system of photogrammetry. Results show that the flexure joints can be modelled by perfect spherical joints due to the small workspace of the telescope. As for the mobile platform deformation, the developed models allow us to explain how the model errors are directly accounted in the parameter identification during the experimental calibration. This results in different sets of identified parameter values which all enable a good positioning accuracy. Those differences are explained and results of calibration allow a proper choice of the most suitable model for the telescope. Considering this model, a positioning accuracy of some micrometers is finally reached.

Key-words: Calibration; Sources of inaccuracy; Flexure joints; Micrometer accuracy; Photogrammetry; Observability; Parallel robots ; Space telescope

This work was supported by Thales Alenia Space and the Region "Provence-Alpes-Côte-d'Azur".

* Includes a detailed explanation of the Jacobian-based model

RESEARCH CENTRE
SOPHIA ANTIPOLIS – MÉDITERRANÉE

2004 route des Lucioles - BP 93
06902 Sophia Antipolis Cedex

Étalonnage expérimental d'un télescope d'observation spatial actif utilisant des liaisons flexibles

Résumé : Afin d'obtenir une précision micrométrique, un modèle complet d'un télescope spatial doit être développé et validé par un processus d'étalonnage. Pour notre application, la dynamique du télescope est lente et donc seul un étalonnage géométrique et/ou statique peut être considéré. De plus, les mesures pour l'étalonnage sont réalisées en salle blanche dans des conditions de pression, de température et d'humidité régulées, ce qui permet de minimiser l'influence des sources d'erreur non géométriques. Ainsi, deux sources d'erreur statique possibles ont été identifiées et modélisées : la déformation de la plateforme mobile et le comportement des joints flexibles. Leurs influences sur la précision du télescope sont comparées à travers un processus d'étalonnage utilisant un moyen de mesure précis de photogrammétrie. Les résultats montrent que les joints flexibles peuvent être modélisés par des rotules parfaites dans le faible espace de travail du télescope. En ce qui concerne la déformation de la plateforme mobile, les modèles développés permettent d'expliquer comment les erreurs de modèle sont directement prises en compte dans l'identification des paramètres. Ceci conduit à différent jeux de paramètres identifiés qui permettent tous d'obtenir une bonne précision finale de positionnement. Ces différences sont expliquées et les résultats d'étalonnage nous permettent de choisir le modèle le plus approprié pour le télescope. Ce modèle permet d'obtenir une précision finale de quelques micromètres.

Mots-clés : Étalonnage ; Sources d'erreur ; Joints flexibles ; Précision micrométrique ; Photogrammétrie ; Observabilité ; Robots parallèles ; Télescope spatial

Contents

1 INTRODUCTION

Robotic calibration aims at improving the robot accuracy through identification of its model parameters. However, the robot model can only approximate the real robot behaviour. Indeed, many sources of inaccuracy influence the functioning of the robot. The classically considered inaccuracy sources are geometric, static, dynamic and/or non-geometric errors due to environmental interactions. Identifying all the inaccuracy sources, if possible, leads to the use of a huge number of specific sensors. For example, static calibration is often performed using force or frequency sensors [1, 2]. Because of the cost and difficulty of such a procedure, many studies were performed to analyse the main sources of inaccuracy that need to be considered in the robot modelling [3, 4, 5]. However, these analyses conclude that influence of systematic errors on the robot accuracy mostly depend on the robot application, manufacturing tolerances and environmental conditions, which means that no *a priori* can be given on the influence of one or another inaccuracy source.

Thus, for calibration of a specific robot, certain assumptions have to be made on the inaccuracy sources that need to be considered. Such assumptions can be derived from the specific environmental conditions or from results of previous work dealing with the same robot architecture or the same applications. Following this, specific measurement systems need to be considered.

The objective of this report is to find the most appropriate model of an active space telescope in order to reach a micrometer accuracy. A space telescope does not manipulate any payload, has a small workspace and does not need high velocity, thus dynamic errors do not need to be considered. Moreover, in order to reduce the influence of the non-geometric errors, measurements for calibration will be performed in a clean room under controlled pressure, temperature and humidity conditions. Thus only geometric and static errors have to be considered for the telescope modelling.

The telescope requires the use of flexure joints to be compatible with space environments. In order to model the flexure joints behaviour, it was found that their parasitic shift and generated stress have to be considered [6]. Parasitic shift occurs when the flexure joint is bent: because of large deflections, the center of rotation of the joint changes during the motion which induces deviations from ideal pivot kinematics. However, such displacements are often small, and so the model parameters often non-identifiable. Concerning the generated stress, a stiffness modelling of the device is required in order to calculate the structure deformation. Nonetheless, small changes in the stiffness parameters can yield to great variations of forces and torques which directly influence the device deformation calculation. Because of the two above drawbacks, flexure joints are often used for micro-manipulation, where high accuracy over only a small workspace is required, as in [6,7]. However, a proper design of the joints [8] allows to consider larger workspaces of some millimetres while keeping a good accuracy considering proper models of deformation. Fazenda *et al.* use neural-network calibration to reach a sub-micrometer accuracy [9]. Dong *et al.* consider stiffness matrices of the joints to simulate the control of a wide-range flexure hinge-based parallel manipulator [10]. Cléroux and Gosselin [11] simulate a calibration process to identify non-geometric parameters in semi-flexible parallel robots.

In this report is proposed three incremental models to consider the flexure joints behaviour of the telescope: a spherical joint model, one issued from equations of the beam theory and a stiffness model. However, it was found that the generated stresses of the flexure joints imply a deformation of the telescope mobile platform, that also needs to be considered in the telescope modelling.

In order to allow the models comparison, the values of the model parameters have to be optimized in order to improve the telescope accuracy. Indeed, because of manufacturing and assembly errors, the model parameter values are not well-known and need to be estimated through

additional measurements: this is the goal of calibration. The way those redundant measurements are obtained defines three types of calibration: external [12, 13, 14, 15, 16, 17], constrained [18, 19, 20] or self-calibration [21, 22, 23]. Constrained calibration does not ensure the manipulator accuracy over the entire workspace [24] and self-calibration is required only if the device has to be calibrated while working. Thus we choose to perform external calibration for the telescope. Photogrammetry is chosen as a measurement system because of its high accuracy over a wide number of object points, which allows to reach a micrometer final accuracy.

The space telescope is presented in section 2. Two models are proposed for the mobile platform deformation in section 3: a linear and a matrix approximation. As for the flexure joints, their parasitic shift are modelled in section 4 and their generated stress is taken into account in the stiffness model of section 5. Finally, the experimental setup of calibration is explained in section 6 and results are analysed and compared in section 7.

2 ACTIVE SPACE TELESCOPE

In this section we describe the active space telescope under consideration. First its application for space observation is explained. Then, its parallel kinematic structure and the definition of notations are given in section 2.2. Finally, requirements for the telescope to provide the required image quality are provided and the use of flexure joints is explained.

2.1 Telescope functioning

The telescope under consideration will be used for space observation. It is composed of two mirrors and as shown in figure 1, the image of the object is reflected in the two mirrors before being view by the camera. Thus the quality of the image greatly depends on the positioning of the secondary mirror (M2) with respect to the primary one (M1). In order reach a micrometer positioning accuracy, a parallel kinematic structure is considered to link M1 and M2, as described in section 2.2.

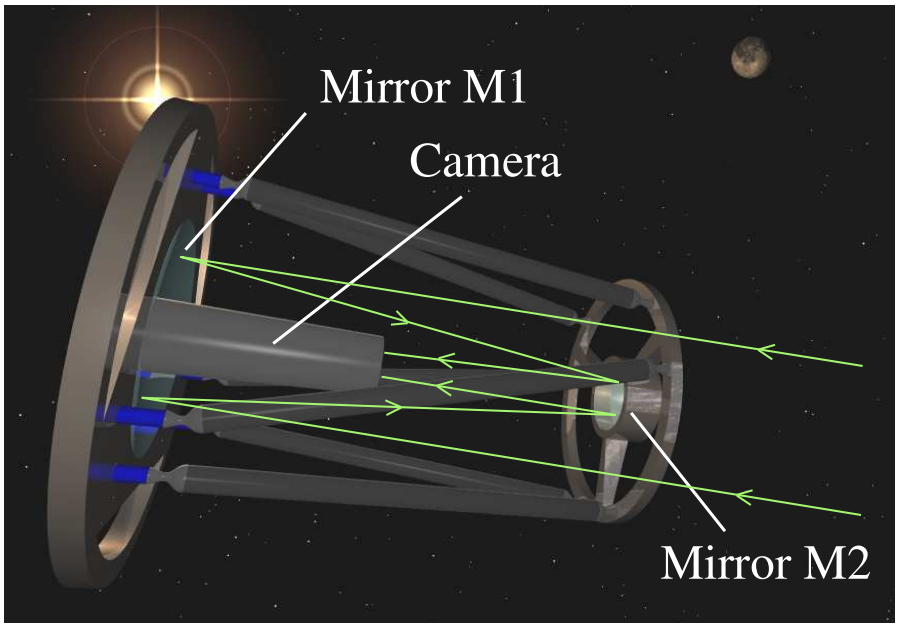

Figure 1: Space telescope for observation

2.2 Kinematic structure

The telescope structure is based on an active wrist platform shown on figure 2, first designed by Merlet [25, 26]. The device thus looks like a 6-PUS parallel robot with all prismatic actuators linked to the base and in a vertical position, where P, U and S stand for prismatic, universal and spherical joints respectively.

Frames $\mathcal{F}_o = (\mathbf{x}_o, \mathbf{y}_o, \mathbf{z}_o)$ and $\mathcal{F}_E = (\mathbf{x}_E, \mathbf{y}_E, \mathbf{z}_E)$ are attached to the base and the mobile platform respectively. Those frames are linked together through a position vector $\mathbf{p}$ and a rotation matrix $\mathbf{R}$ which describe the position and orientation of the mobile platform with respect to the base.

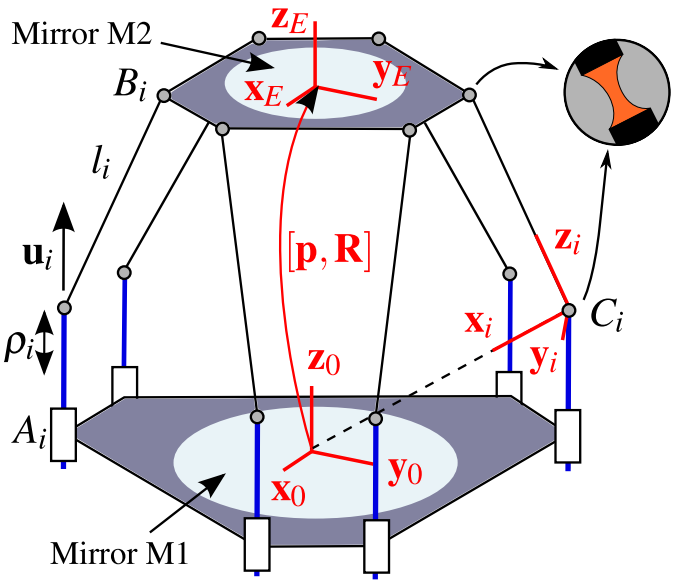

Figure 2: Kinematic structure of the space telescope

The base and mobile platforms are linked together through 6 legs of fixed length $l_i \approx 0.5$ m, with $i = 1...6$. Each leg i is attached at one side to the mobile platform at point $\mathbf{b}_i$, whose coordinates are given in the mobile frame $\mathcal{F}_E$, and to point $\mathbf{c}_i$ at the other side. Coordinates of point $\mathbf{c}_i$ are always given in the base frame $\mathcal{F}_o$ and follow the relation $\mathbf{c}_i = \mathbf{a}_i + \rho_i \mathbf{u}_i$ where ρ_i relates the displacement of actuator i along direction $\mathbf{u}_i$ and $\mathbf{a}_i$ stands for the attachment point of the i^{th} actuator on the base platform. To each leg i is attached a frame $\mathcal{F}_i = (\mathbf{x}_i, \mathbf{y}_i, \mathbf{z}_i)$, where $\mathbf{z}_i$ is the principal direction of the leg and $\mathbf{x}_i$ is such as $\mathbf{z}_o$ belongs to the plane $(\mathbf{c}_i, \mathbf{x}_i, \mathbf{z}_i)$.

The initial pose $\mathbf{X}^0$ of the device is defined as the position $\mathbf{p}^0$ and orientation $\mathbf{R}^0$ of the mobile platform where all the actuators are at their initial position ρ_i^0. In this pose, the orientation of frame $\mathcal{F}_i$ with respect to $\mathcal{F}_o$ is $\mathbf{R}_i^0 = [\mathbf{x}_i^0\ \mathbf{y}_i^0\ \mathbf{z}_i^0]$.
The design geometry is given in figure 3, with design parameters α_0, r_0, α_E and r_E.

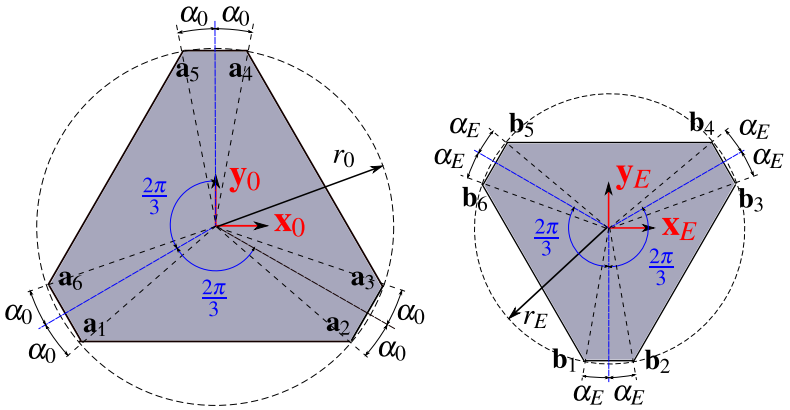

Figure 3: Geometry of the base and the mobile platforms

2.3 Telescope requirements

The space telescope does not manipulate any payload and only needs a small workspace. The device workspace W and desired accuracy are given in table 1. Workspace requirements of the telescope do not consider θ_z since motions around $\mathbf{z}_E$ do not influence its functioning.

	x (mm)	y (mm)	z (mm)	θ_x (°)	θ_y (°)
Workspace	2	2	0.2	1	1
Desired Accuracy	0.1	0.1	0.01	0.05	0.05

Table 1: Requirements of the telescope

For the telescope to fit the workspace requirements, the motor ranges are set to $\Delta\rho_i = \pm 1.3$ mm with an accuracy of ± 1 μm. Considering a perfect 6-PUS parallel robot with dimensions of figure 3 and noting the above motor specifications, a pose accuracy of, at worst, 6 μm and 10^{-6} degree was calculated over the entire workspace W.

2.4 Flexure joints

In order to avoid backlash, friction, hysteresis effects, to improve the device repeatability and for the telescope to be compatible with the aerospace environment [27], circular-fillet hinge flexure joints [28] are considered in place of U and S joints, as shown in orange on figure 2. Even if flexure joints are of interest for the manipulator design, two major drawbacks penalize the device accuracy: generated stress and parasitic shift [6] that need to be taken into account in the telescope modelling.

In this report, different models of kinematic and static behaviour of the flexure joints are proposed and compared in order to enhance the manipulator accuracy after calibration. However, an other source of inaccuracy was observed using photogrammetry data. Indeed, the mobile platform of the telescope lose its shape during the telescope functioning and this deformation also needs to be considered in the telescope modelling, as explained in section 3.

3 MOBILE PLATFORM DEFORMATION MODELLING

Photogrammetry was performed on the entire telescope structure as shown in figure 4. For 40 poses, the position of each object point attached to the telescope parts is measured. However, each position is measured in the frame of measurement with noise. Thus, a robust method for pose determination from corresponding data points is required to obtain the rigid body displacement with the best possible accuracy. The data analysis highlights a deformation of the mobile platform. However, it is not possible to change the design of the mobile platform since it directly influences the image quality of the telescope. Consequently, those deformations have to be taken into account: a linear and a matrix model are proposed below.

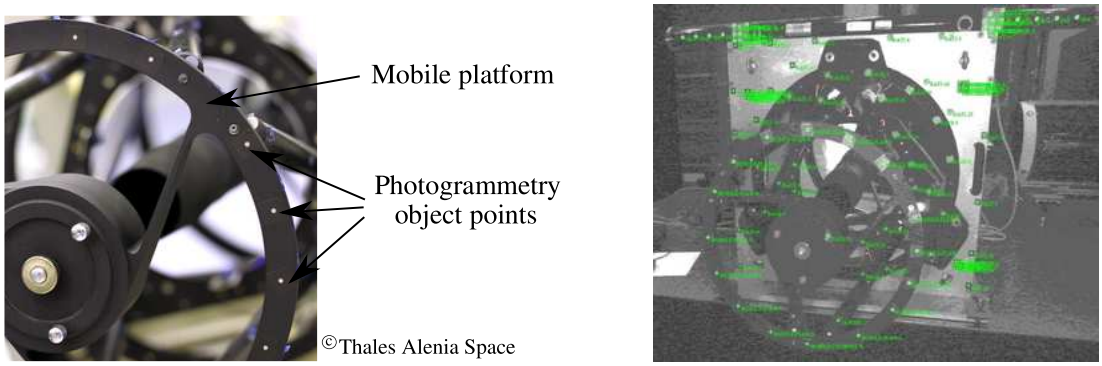

Figure 4: Photo of the telescope mobile platform and photogrammetry data

3.1 Photogrammetry data analysis

In order to extract the position and orientation of each rigid body of the telescope structure from photogrammetry object points, two methods are compared in this section. The first one considers the geometrical shape of the rigid body. The second one is based on the algorithm proposed by Haralick *et al.* [29]. To allow the comparison and without loss of generality, let consider a cylinder on which is fixed a variable number of object points.

The first algorithm finds the position and direction of the straight line that minimizes the sum of square distances to the object points. The orientation of this line defines the $\mathbf{z}_i$ axis. The projection of the barycentre of the object points on this line gives the position of the rigid body and the direction of this projection the $\mathbf{x}_i$ axis.

Contrary to the first algorithm, the Haralick method gives only the displacements of a scatter of points between two poses, with noise considerations on each pose. The reader is referred to [29] for the algorithm details. Please note that Haralick *et al.* considers only Gaussian noise of variance σ on each object points. However, simulations with uniformly distributed noise over the range $[-2\sigma; 2\sigma]$ give the same results, for both algorithms.

To process simulations, first a perfect scatter of object points is generated in an initial position $\mathcal{P}_0$. All the object points belong to a cylinder of length 50 mm and radius 1 mm. Simulations are performed for different number of object points, from 6 to 20 as it can be seen on the abscissa of figure 5. Each of those scatters is then translated to a desired pose $\mathcal{P}$ and measurement noise is added to each object points. The measurement noise follows a normal distribution of variance $\sigma = 5$ μm which corresponds to the photogrammetry uncertainties. Finally, the two methods are applied on those scatters in order to calculate the cylinder displacement. For each number

of object points, the process is repeated 20 times. The mean of the errors and their variance are represented on figure 5 as an error bar.

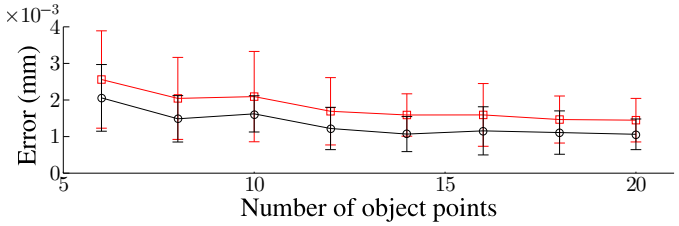

(a) Errors on position

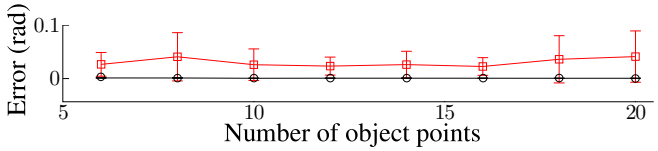

(b) Errors on orientation

Figure 5: Comparison between the first algorithm (red squares) and Haralick method (black circles)

Figure 5 shows that the Haralick method is more robust to measurement noise and presents the advantage to have no a priori knowledge of the body geometry. Thus, this method will be applied on each scatter of object points of the platform in order to obtain its position and orientation in the measurement frame.

With Haralick method, the data analysis shows a deformation of the mobile platform of the telescope. Indeed, deformations of about ten micrometers from a rigid model are observed on almost every measurement configurations.

Figure 6 illustrates a deformation of the ring on which the legs are attached at points $\mathbf{b}_i$. The deformed ring looks like a buckled wheel for almost all measurement configurations. Such a deformation is due to the flexure joints that generate stresses. The measured deformations at points $\mathbf{b}_i$ are higher than the 5 μm given by finite element modelling simulations, and unfortunately above the desired accuracy.

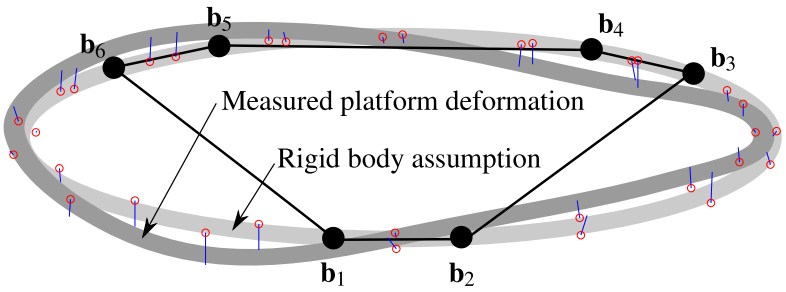

Figure 6: Measured deformation of the mobile platform for one measurement configuration. Blue lines represent the amplified error between the measured object points and their rigid body position estimation (red circle points).

The observed deformations mostly impact the position b_i^z of points $\mathbf{b}_i$ (b_i^x, b_i^y and b_i^z being

the coordinates of $\mathbf{b}_i$ in the mobile platform frame $\mathcal{F}_E$) while having very little influence on the position and orientation of the frame $\mathcal{F}_E$. In order to consider the displacements Δb_i^z of points $\mathbf{b}_i$, two incremental models are proposed below.

3.2 Linear model

Figure 7 shows the plot of the measured displacements Δb_i^z of points $\mathbf{b}_i$ as functions of the actuator displacements $\Delta\rho_i$. Thanks to the small displacements Δb_i^z (± 60 μm), a linear relation between Δb_i^z and $\Delta\rho_i$ is supposed, considering the coefficient κ_i:

$$\Delta b_i^z = \kappa_i \Delta\rho_i \tag{1}$$

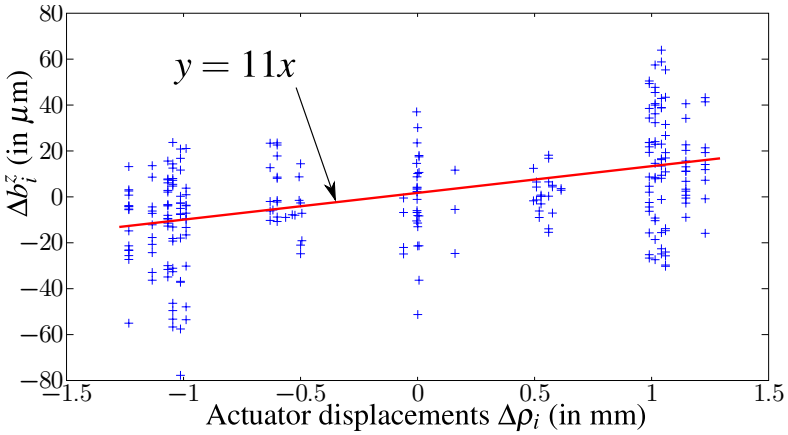

Figure 7: Linear approximation of the platform deformation

The initial value of κ_i is identified to 0.011 for $i = 1...6$.

3.3 Matrix model

The mobile platform deformation is due to the stress generated by the flexure joints. Those stresses depend on the static equilibrium of the mobile platform which involves both forces acting on the platform at points $\mathbf{b}_i$. Moreover, those forces should mostly depend on the actuator displacements $\Delta\rho_i$ that induce deformations of the flexure joints. So displacements of point $\mathbf{b}_i$ must depend on all the actuator displacements such as:

$$\Delta\mathbf{b}^z = \mathbf{K}\Delta\boldsymbol{\rho} \tag{2}$$

with $\Delta\mathbf{b}^z = [\Delta b_1^z ... \Delta b_6^z]^T$, $\Delta\boldsymbol{\rho} = [\Delta\rho_1 ... \Delta\rho_6]^T$ and $\mathbf{K}$ a coefficient matrix.

In order to identify the terms of the coefficient matrix $\mathbf{K}$, data from figure 7 is considered. For each leg i, the i^{th} row $\mathbf{k}_i$ of matrix $\mathbf{K}$ is used to calculate the displacements Δb_i^z such as:

$$\Delta b_i^z = \mathbf{k}_i \Delta\boldsymbol{\rho} \tag{3}$$

The objective is to obtain the best estimate of Δb_i^z using equation (3) considering the measurements of figure 7. In order to minimize the distances between the measurements and the

matrix estimate, a least-square optimization is performed on each leg of the telescope. The identified matrix is given in equation 4.

$$\mathbf{K} = 10^{-3} \begin{bmatrix} 16 & 0 & -8 & 12 & -2 & -20 \\ 0 & 20 & -17 & -1 & 13 & -13 \\ -2 & -15 & 14 & 2 & -9 & 9 \\ 6 & -12 & 4 & 14 & -16 & 2 \\ -12 & 7 & 0 & -15 & 14 & 4 \\ -20 & -1 & 10 & -10 & 2 & 19 \end{bmatrix} \tag{4}$$

The elements of $\mathbf{K}$ are of the same order of magnitude as κ_i. Analysing matrix $\mathbf{K}$, a strong dependency between legs 1-6, 2-3, and 4-5 are observed. For example, displacements $\Delta\rho_1$ and $\Delta\rho_6$ greatly influence Δb_1^z and Δb_6^z. This may be due to the mobile platform geometry. Indeed, as shown in figure 4, there is no strengthening for the mobile platform ring between the attachment points of legs 1 and 6. Thus displacements of point $\mathbf{b}_1$ can have a significant impact on Δb_6^z.

Considering the matrix model, the maximal committed error on the displacement estimation of Δb_i^z is 20 μm, and the average error is 5 μm which is close to the measurement noise.

With both the linear and matrix models, the mobile platform deformation can be taken into account in the telescope modelling setting $\mathbf{b}_i^* = \mathbf{b}_i + \Delta b_i^z \mathbf{z}_o$. This allows to consider the mobile platform as a rigid body while modelling the telescope. In order to take into account the behaviour of the flexure joints, kinematic models and a stiffness model are proposed in sections 4 and 5 respectively.

4 KINEMATIC MODELS

In this section, only the kinematic behaviour of the telescope is considered. The impact of internal forces over the entire structure is neglected and the manipulator parts are treated as rigid bodies thanks to the previous models of the mobile platform deformation. For the two first models, flexure joints are supposed to behave as perfect spherical joints.

4.1 6-PUS model

Considering leg orientations $\mathbf{z}_i$ of a 6-PUS, geometrical closed-loop equations can be written for each leg i:

$$\mathbf{p} + \mathbf{R}\mathbf{b}_i^* = \mathbf{a}_i + \rho_i \mathbf{u}_i + l_i \mathbf{z}_i \tag{5}$$

The device inputs can then be issued from equation (5):

$$\rho_i = (\mathbf{p} + \mathbf{R}\mathbf{b}_i^* - \mathbf{a}_i - l_i \mathbf{z}_i)^T \mathbf{u}_i \tag{6}$$

However, equation (6) considers the leg orientation $\mathbf{z}_i$ which need information on the motor input ρ_i to be calculated. Even if it can be done using an iterative algorithm, motor inputs can also be derived from equation (7).

$$\begin{array}{ll} & l_i = \|\mathbf{p} + \mathbf{R}\mathbf{b}_i^* - \mathbf{a}_i - \rho_i \mathbf{u}_i\| \\ \longrightarrow & \rho_i = \mathbf{h}_i^T \mathbf{u}_i - \sqrt{(\mathbf{h}_i^T \mathbf{u}_i)^2 - (\|\mathbf{h}_i\|^2 - l_i^2)} \\ \text{with} & \mathbf{h}_i = \mathbf{p} + \mathbf{R}\mathbf{b}_i^* - \mathbf{a}_i \end{array} \tag{7}$$

4.2 Jacobian-based model

Differentiating equation (5) with respect to time yields to the inverse of the kinematic Jacobian matrix $\mathbf{J}(\mathbf{X})$ such as $\dot{\boldsymbol{\rho}} = \mathbf{J}^{-1}(\mathbf{X})\dot{\mathbf{X}}$ where $\dot{\boldsymbol{\rho}}$ is the vector of actuators velocities, $\dot{\mathbf{X}}$ is the twist of the mobile platform and $\mathbf{X} = [\mathbf{p}^T, \theta\mathbf{v}^T]^T$ with $\mathbf{v}$ the rotation axis vector and θ the rotation angle of the rotation matrix $\mathbf{R}$ [24]:

$$\mathbf{J}^{-1}(\mathbf{X}) = \begin{bmatrix} \dfrac{\mathbf{z}_1^T}{\mathbf{u}_1^T \mathbf{z}_1} & (\mathbf{R}\mathbf{b}_1^*)^T \times \dfrac{\mathbf{z}_1^T}{\mathbf{u}_1^T \mathbf{z}_1} \\ \vdots & \vdots \\ \dfrac{\mathbf{z}_i^T}{\mathbf{u}_i^T \mathbf{z}_i} & (\mathbf{R}\mathbf{b}_i^*)^T \times \dfrac{\mathbf{z}_i^T}{\mathbf{u}_i^T \mathbf{z}_i} \\ \vdots & \vdots \end{bmatrix}_{6\times 6} \tag{8}$$

For small displacements, the typical assumption $\delta\boldsymbol{\rho} = \mathbf{J}^{-1}(\mathbf{X})\delta\mathbf{X}$ can be made. Moreover, because of the small workspace of the telescope, the Jacobian matrix does not vary too much and thus can be approximated by the Jacobian matrix of the initial pose of the device $\mathbf{J}_0 = \mathbf{J}(\mathbf{X}^0)$. Thus the kinematic behaviour of the telescope can be approximated with equation (9) [30].

$$\boldsymbol{\rho} = \boldsymbol{\rho}^0 + \mathbf{J}_0^{-1}(\mathbf{X} - \mathbf{X}^0) \tag{9}$$

4.3 Beam theory-based model

In order to consider the parasitic shift of the flexure joints, their displacements are estimated using equations from the beam theory. Flexure joints are assumed to be equivalent to circular beams, as shown on figure 8.

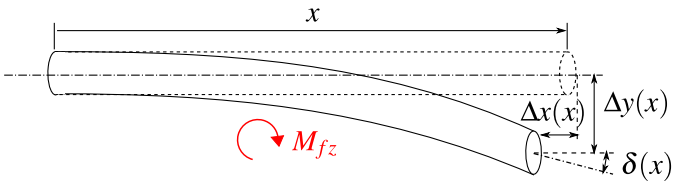

Figure 8: Beam theory model of a flexure joint and its deformations

As usual in beam theory, the principal deflection is assumed to be generated by the bending moment M_{fz}. Considering the Euler-Bernoulli hypothesis, the static beam equations can be derived, with E, I_{Gz} and γ being the Young modulus, the second moment of area and the curvature of the flexure joints respectively:

$$\left\{\begin{array}{rl} M_{fz} = EI_{Gz}\ \gamma & \\ \Delta y(x) = \dfrac{M_{fz}}{EI_{Gz}}\dfrac{x^2}{2} & \longrightarrow \quad \Delta y(x) = \gamma\ \dfrac{x^2}{2} \end{array}\right. \tag{10}$$

Then, the length $l(x)$ of the deformed beam can be calculated using equation (11):

$$\begin{array}{rl} l(x) = & \displaystyle\int_0^x \sqrt{1+\Delta y'(x)^2}\,\mathrm{d}x \\ \longrightarrow \quad \Delta x(x) = & \displaystyle\int_0^x \sqrt{1+(\gamma x)^2}\,\mathrm{d}x\ -\ x \end{array} \tag{11}$$

Considering the workspace of the telescope, a flexure joint of length l_b cannot be bent at an angle more than $\delta = 1°$ from its home position. For such small deflections, the orientation δ can be approximated by $\delta = \gamma\ l_b$. Thus the beam displacements Δy and Δx can be calculated using equation (12):

$$\left\{\begin{array}{l} \Delta y = \Delta y(l_b) = \dfrac{l_b}{2}\delta \\ \Delta x = \Delta x(l_b) = l_b\left(\dfrac{\delta\sqrt{1+\delta^2}+\sinh^{-1}(\delta)}{2\delta} - 1\right) \end{array}\right. \tag{12}$$

Writing and analysing the Taylor series expansion of equation (12) leads to:

$$\left(\Delta x - \frac{3}{4}l_b\right)^2 + \Delta y^2 = \left(\frac{3}{4}l_b\right)^2 + o(\delta^4) \tag{13}$$

which is the equation of a circle with center $(\frac{3}{4}l_b, 0)$ and radius $\frac{3}{4}l_b$. Both the ideal kinematic pivot of center $(\frac{1}{2}l_b, 0)$ and radius $\frac{1}{2}l_b$, the beam theory-based model kinematic and its identification as circle of equation (13) are plotted on figure 9 for $\delta \in [0; 1°]$.

Figure 9 shows that the kinematic displacement of the flexure joints in their planes of deformation is perfectly identified by the circle of equation 13. However, their orientations are equal to that of an ideal pivot for the same Δy.

In order to consider the displacements and orientations of the flexure joints, a kinematic model is proposed in figure 10, where l_{bi} is the length of the flexure joints of leg i and β_i a design parameter whose initial value is fixed to $\frac{1}{4}$. Displacements are constrained on a sphere of radius $(1-\beta_i)l_{bi}$ while orientations are the same as an ideal spherical joint at $\mathbf{a}_i + \rho_i\mathbf{u}_i$, with $\mathbf{z}_i^0$ the initial orientation of the flexure joints of leg i.

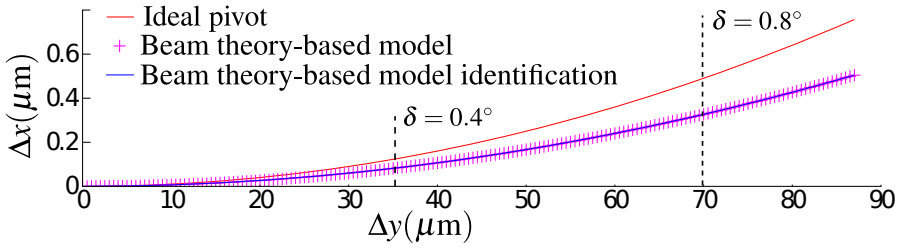

Figure 9: Displacement of a flexure joint considering ideal pivot and beam theory-based model kinematics for $\delta \in [0; 1°]$

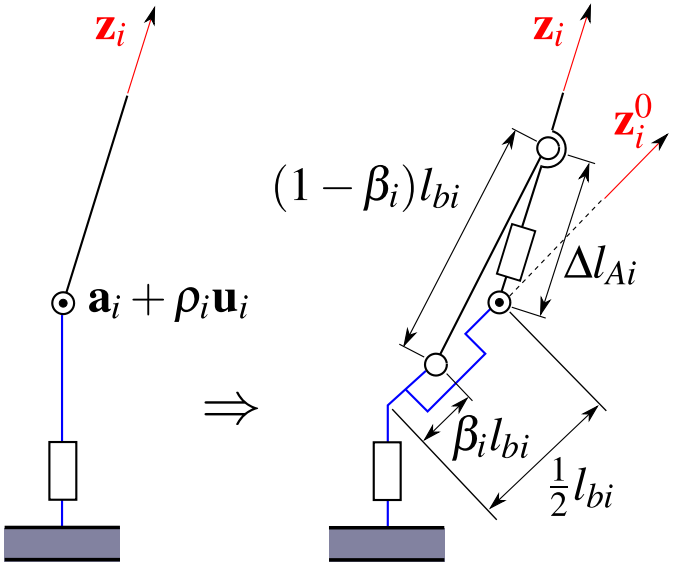

Figure 10: Kinematic model of a flexure joint

Considering the kinematic model of figure 10, the closed-loop equation for each leg i becomes:

$$\mathbf{p} + \mathbf{R}\mathbf{b}_i^* - \mathbf{a}_i - \rho_i \mathbf{u}_i = (l_i - l_{bi} + \Delta l_{Ai} + \Delta l_{Bi})\mathbf{z}_i \tag{14}$$

with Δl_{Ai} and Δl_{Bi} the displacements of the flexure joints of leg i attached to the base and to the mobile platform respectively.
Writing the shortest kinematic closed loop equation involving Δl_{Ai} leads to:

$$\begin{aligned} & (1-\beta_i) l_{b_i} = \|(\tfrac{1}{2} - \beta_i) l_{b_i} \mathbf{z}_i^0 + \Delta l_{Ai} \mathbf{z}_i\| \\ \longrightarrow \quad & (1-\beta_i)^2 l_{b_i}^2 = (\tfrac{1}{2} - \beta_i)^2 l_{b_i}^2 + 2(\tfrac{1}{2} - \beta_i) l_{b_i} \Delta l_{Ai} \mathbf{z}_i^T \mathbf{z}_i^0 + \Delta l_{Ai}^2 \\ \longrightarrow \quad & \Delta l_{Ai}^2 + (1-2\beta_i) l_{b_i} \mathbf{z}_i^T \mathbf{z}_i^0 \Delta l_{Ai} + (\beta_i - \tfrac{3}{4}) l_{b_i}^2 = 0 \end{aligned} \tag{15}$$

The quadratic equation (15) has only one positive solution for Δl_{Ai}:

$$\Delta l_{Ai} = \frac{l_{b_i}}{2} \left((2\beta_i - 1)\mathbf{z}_i^T \mathbf{z}_i^0 + \sqrt{3 - 4\beta_i + \left((1-2\beta_i)\mathbf{z}_i^T \mathbf{z}_i^0\right)^2} \right) \tag{16}$$

Almost the same equation can be found considering Δl_{Bi}:

$$\Delta l_{Bi} = \frac{l_{b_i}}{2} \left((2\beta_i - 1)\mathbf{z}_i^T \mathbf{R}\mathbf{z}_i^0 + \sqrt{3 - 4\beta_i + \left((1-2\beta_i)\mathbf{z}_i^T \mathbf{R}\mathbf{z}_i^0\right)^2} \right) \tag{17}$$

Considering equations (14), (16), (17) and noting that $\mathbf{z}_i$ is a unit vector yields to a system of algebraic equations in the unknowns ρ_i, $\mathbf{z}_i$, Δl_{Ai} and Δl_{Bi}:

$$\begin{cases} \mathbf{p} + \mathbf{R}\mathbf{b}_i^* - \mathbf{a}_i - \rho_i \mathbf{u}_i = (l_i - l_{bi} + \Delta l_{Ai} + \Delta l_{Bi})\mathbf{z}_i \\ \left(\dfrac{2\Delta l_{Ai}}{l_{bi}} + (1-2\beta_1)\mathbf{z}_i^T \mathbf{z}_i^0 \right)^2 = 3 - 4\beta_i + \left((1-2\beta_i)\mathbf{z}_i^T \mathbf{z}_i^0\right)^2 \\ \left(\dfrac{2\Delta l_{Bi}}{l_{bi}} + (1-2\beta_1)\mathbf{z}_i^T \mathbf{R}\mathbf{z}_i^0 \right)^2 = 3 - 4\beta_i + \left((1-2\beta_i)\mathbf{z}_i^T \mathbf{R}\mathbf{z}_i^0\right)^2 \\ \|\mathbf{z}_i\|^2 = 1 \end{cases} \tag{18}$$

Equations (14) are linear in $\mathbf{z}_i$, which give one linear equation in the ρ_i that can be solved. The two remaining equations involving Δl_{Ai} and Δl_{Bi} are of global degree 8 and 7 respectively. Using interval analyses, the uniqueness of the solution in the neighbourhood of the nominal values of Δl_{Ai} and Δl_{Bi} has been proved. This allows us to use iterations of Newton-Raphson for rapid calculation of the inverse kinematics of the beam theory-based model.

5 STIFFNESS MODEL

The parasitic shift of the flexure joints is considered thanks to equations of the beam theory. However, the pose of the telescope mobile platform also depends on its static equilibrium. The static equilibrium of the platform is written in equation (19), $\tilde{\mathbf{P}}_E$ being the external load acting at the center of the mobile platform, $\tilde{\mathbf{P}}^i_{\mathbf{b}'}$ the load generated by the flexure joints acting on the mobile platform and $\mathbf{M}_i$ a 6×6 matrix taking into account the momentum transport:

$$\tilde{\mathbf{P}}_E + \sum_{i=1}^{6} \mathbf{M}_i \tilde{\mathbf{P}}^i_{\mathbf{b}'} = \mathbf{0} \tag{19}$$

Stresses generated by the flexure joints are functions of their deformations. Thus, the stiffness matrices of the flexure joints need to be derived for their deformation influence on the static equations of the mobile platform to be considered.

5.1 Local stiffness matrix of a flexure joint

Flexure joints of the telescope can be assimilated as perfect cylinders of small ratio diameter/length as shown on figure 11. Hence, stiffness matrices can be calculated from the finite element analysis theory as it is done by Dong *et al.* in [10].

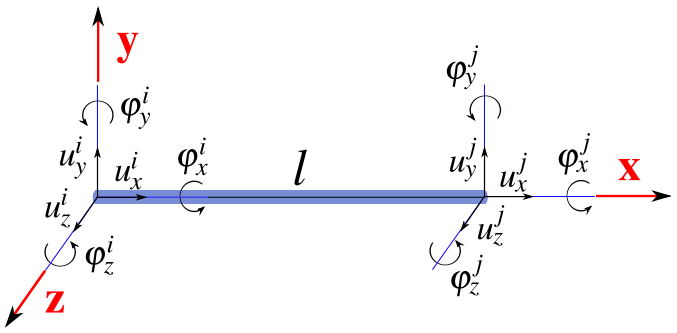

Figure 11: Local coordinate system of a flexure joint

The stiffness matrix $\mathbf{K}_{loc}$ links together the nodal loads $[\mathbf{P}_i^T, \mathbf{P}_j^T]^T$ and displacements $[\mathbf{u}_i^T, \mathbf{u}_j^T]^T$ of the beam through equation (20):

$$\begin{bmatrix} \mathbf{P}_i \\ \mathbf{P}_j \end{bmatrix} = \mathbf{K}_{loc} \begin{bmatrix} \mathbf{u}_i \\ \mathbf{u}_j \end{bmatrix} \tag{20}$$

with $\mathbf{P}_i = [F_x^i, F_y^i, F_z^i, M_x^i, M_y^i, M_z^i]^T$ and $\mathbf{u}_i = [u_x^i, u_y^i, u_z^i, \varphi_x^i, \varphi_y^i, \varphi_z^i]^T$, $(\varphi_z^i, \varphi_y^i, \varphi_x^i)$ being the ZYX-Euler angles (same for j).

Considering a beam element of length l, of sectional area S, of Young's and shear modulus E and G, and of rotational and polar moment of inertia I and J, the stiffness matrix can be expressed through equation (21), with $k_1 = EI$, $k_2 = ES$ and $k_3 = GJ$.

$$\mathbf{K}_{loc} = \begin{bmatrix} \mathbf{K}_{11} & \mathbf{K}_{12} \\ \mathbf{K}_{21} & \mathbf{K}_{22} \end{bmatrix}_{12\times12} \tag{21}$$

with

$$\mathbf{K}_{11} = \frac{1}{l}\begin{bmatrix} k_2 & 0 & 0 & 0 & 0 & 0 \\ 0 & \frac{12k_1}{l^2} & 0 & 0 & 0 & \frac{6k_1}{l} \\ 0 & 0 & \frac{12k_1}{l^2} & 0 & -\frac{6k_1}{l} & 0 \\ 0 & 0 & 0 & k_3 & 0 & 0 \\ 0 & 0 & -\frac{6k_1}{l} & 0 & 4k_1 & 0 \\ 0 & \frac{6k_1}{l} & 0 & 0 & 0 & 4k_1 \end{bmatrix}_{6\times 6}$$

$$\mathbf{K}_{12} = \frac{1}{l}\begin{bmatrix} -k_2 & 0 & 0 & 0 & 0 & 0 \\ 0 & -\frac{12k_1}{l^2} & 0 & 0 & 0 & \frac{6k_1}{l} \\ 0 & 0 & -\frac{12k_1}{l^2} & 0 & -\frac{6k_1}{l} & 0 \\ 0 & 0 & 0 & -k_3 & 0 & 0 \\ 0 & 0 & -\frac{6k_1}{l} & 0 & 2k_1 & 0 \\ 0 & \frac{6k_1}{l} & 0 & 0 & 0 & 2k_1 \end{bmatrix}_{6\times 6}$$

$$\mathbf{K}_{21} = \frac{1}{l}\begin{bmatrix} -k_2 & 0 & 0 & 0 & 0 & 0 \\ 0 & -\frac{12k_1}{l^2} & 0 & 0 & 0 & -\frac{6k_1}{l} \\ 0 & 0 & -\frac{12k_1}{l^2} & 0 & \frac{6k_1}{l} & 0 \\ 0 & 0 & 0 & -k_3 & 0 & 0 \\ 0 & 0 & \frac{6k_1}{l} & 0 & 2k_1 & 0 \\ 0 & -\frac{6k_1}{l} & 0 & 0 & 0 & 2k_1 \end{bmatrix}_{6\times 6}$$

$$\mathbf{K}_{22} = \frac{1}{l}\begin{bmatrix} k_2 & 0 & 0 & 0 & 0 & 0 \\ 0 & \frac{12k_1}{l^2} & 0 & 0 & 0 & -\frac{6k_1}{l} \\ 0 & 0 & \frac{12k_1}{l^2} & 0 & \frac{6k_1}{l} & 0 \\ 0 & 0 & 0 & k_3 & 0 & 0 \\ 0 & 0 & \frac{6k_1}{l} & 0 & 4k_1 & 0 \\ 0 & -\frac{6k_1}{l} & 0 & 0 & 0 & 4k_1 \end{bmatrix}_{6\times 6}$$

5.2 Inverse stiffness model

For ease of calculation, each leg l_i of the device is considered as a rigid beam of stiffness matrix $\mathbf{K}^l$ depending of the form and material property of the legs, and each flexure joint is identified as a stiffness matrix $\mathbf{K}^b$. The stiffness model of one chain of the device is presented in figure 12. Note that contrary to the kinematic models of section 4 where points $\mathbf{b}_i$ and $\mathbf{c}_i$ relates to the center of the spherical joints while $\mathbf{a}_i$ is attached to the base, here points $\mathbf{a}'_i$, $\mathbf{b}'_i$, $\mathbf{c}'_i$ and $\mathbf{d}'_i$ all stands for nodes of the flexure joints. Thus we have the following relations:

$$\begin{cases} \mathbf{a}'_i = (\mathbf{a}_i + \rho_i \mathbf{u}_i) - \frac{1}{2} l_{bi} \mathbf{z}_i^0 \\ \mathbf{b}'_i = \mathbf{b}_i^* + \frac{1}{2} l_{bi} \mathbf{z}_i^0 \\ \mathbf{c}'_i = \mathbf{c}_i + \frac{1}{2} l_{bi} \mathbf{z}_i^0 \\ \mathbf{d}'_i = \mathbf{b}_i^* - \frac{1}{2} l_{bi} \mathbf{z}_i^0 \end{cases} \tag{22}$$

Considering figure 12, the total local stiffness matrix of each chain i follows equation (23) and can be calculated (suffix i is omitted for clarity reasons):

$$\begin{bmatrix} \mathbf{P}_{\mathbf{a}'} \\ \mathbf{P}_{\mathbf{c}'} \\ \mathbf{P}_{\mathbf{d}'} \\ \mathbf{P}_{\mathbf{b}'} \end{bmatrix} = \mathbf{K} \begin{bmatrix} \mathbf{u}_{\mathbf{a}'} \\ \mathbf{u}_{\mathbf{c}'} \\ \mathbf{u}_{\mathbf{d}'} \\ \mathbf{u}_{\mathbf{b}'} \end{bmatrix} \tag{23}$$

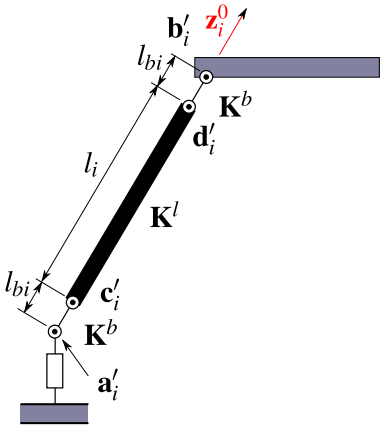

Figure 12: Stiffness model of one chain of the device

with

$$\mathbf{K} = \begin{bmatrix} \mathbf{K}_{11}^d & \mathbf{K}_{12}^d & & \\ \mathbf{K}_{21}^d & \mathbf{K}_{22}^d + \mathbf{K}_{11}^l & \mathbf{K}_{12}^l & \\ & \mathbf{K}_{21}^l & \mathbf{K}_{22}^l + \mathbf{K}_{11}^d & \mathbf{K}_{12}^d \\ & & \mathbf{K}_{21}^d & \mathbf{K}_{22}^d \end{bmatrix}_{24\times 24} \tag{24}$$

Then equations (23) and (24) can be written by regrouping the known and the unknown parameters [31]: $\mathbf{P}_{kno} = [\mathbf{P}_{\mathbf{c}'}^T, \mathbf{P}_{\mathbf{d}'}^T]^T$, $\mathbf{P}_{unk} = [\mathbf{P}_{\mathbf{a}'}^T, \mathbf{P}_{\mathbf{b}'}^T]^T$, $\mathbf{u}_{kno} = [\mathbf{u}_{\mathbf{a}'}^T, \mathbf{u}_{\mathbf{b}'}^T]^T$ and $\mathbf{u}_{unk} = [\mathbf{u}_{\mathbf{c}'}^T, \mathbf{u}_{\mathbf{d}'}^T]^T$.

$$\begin{bmatrix} \mathbf{P}_{kno} \\ \mathbf{P}_{unk} \end{bmatrix} = \begin{bmatrix} \mathbf{K}_u & \mathbf{K}_f \\ \mathbf{K}_f^T & \mathbf{K}_c \end{bmatrix} \begin{bmatrix} \mathbf{u}_{unk} \\ \mathbf{u}_{kno} \end{bmatrix} \tag{25}$$

$$\begin{aligned} \text{with } \mathbf{K}_u &= \begin{bmatrix} \mathbf{K}_{22}^d + \mathbf{K}_{11}^l & \mathbf{K}_{12}^l \\ \mathbf{K}_{21}^l & \mathbf{K}_{22}^l + \mathbf{K}_{11}^d \end{bmatrix}, \\ \mathbf{K}_f = \begin{bmatrix} \mathbf{K}_{21}^d & \\ & \mathbf{K}_{12}^d \end{bmatrix} &\text{ and } \mathbf{K}_c = \begin{bmatrix} \mathbf{K}_{11}^d & \\ & \mathbf{K}_{22}^d \end{bmatrix} \end{aligned} \tag{26}$$

Since $\mathbf{P}_{\mathbf{c}'}$ and $\mathbf{P}_{\mathbf{d}'}$ are the external loads applied on nodes $\mathbf{c}'$ and $\mathbf{d}'$, we have $\mathbf{P}_{\mathbf{c}'} = \mathbf{P}_{\mathbf{d}'} = \mathbf{0}_{6\times 1}$. Equation (25) thus becomes:

$$\begin{aligned} &\begin{cases} \mathbf{0}_{12\times 1} = \mathbf{K}_u \mathbf{u}_{unk} + \mathbf{K}_f \mathbf{u}_{kno} \\ \mathbf{P}_{unk} = \mathbf{K}_f^T \mathbf{u}_{unk} + \mathbf{K}_c \mathbf{u}_{kno} \end{cases} \\ \longrightarrow \quad &\mathbf{P}_{unk} = \left(\mathbf{K}_c - \mathbf{K}_f^T \mathbf{K}_u^{-1} \mathbf{K}_f\right) \mathbf{u}_{kno} \end{aligned} \tag{27}$$

However, equation (27) is still in the local coordinate system of the chain under consideration. In order to obtain the stiffness equations in the base frame $\mathcal{F}_o$, the initial orientation matrix $\mathbf{R}_i^0$ of the i^{th} leg needs to be considered. Thus the global loads $\tilde{\mathbf{P}}_{unk}^i$ and displacements $\tilde{\mathbf{u}}_{kno}^i$ can be calculated for each leg i through equation (28), with $\mathbf{T}_{i0} = diag(\mathbf{R}_i^0, \mathbf{R}_i^0, \mathbf{R}_i^0, \mathbf{R}_i^0)$ where $diag()$ stands for the block diagonal matrix:

$$\tilde{\mathbf{P}}_{unk}^i = \tilde{\mathbf{K}}^i \ \tilde{\mathbf{u}}_{kno}^i = \mathbf{T}_{i0} \left(\mathbf{K}_c - \mathbf{K}_f^T \mathbf{K}_u^{-1} \mathbf{K}_f\right) \mathbf{T}_{i0}^{-1} \ \tilde{\mathbf{u}}_{kno}^i \tag{28}$$

$$\tilde{\mathbf{P}}_{\mathbf{b}'}^i = \tilde{\mathbf{K}}_{21}^i \ \tilde{\mathbf{u}}_{\mathbf{a}'}^i + \tilde{\mathbf{K}}_{22}^i \ \tilde{\mathbf{u}}_{\mathbf{b}'}^i \tag{29}$$

Analysing equation (29), we see that $\tilde{\mathbf{P}}^i_{\mathbf{b}'}$ is a function of only the unknown $\Delta\rho_i$ in $\tilde{\mathbf{u}}^i_{\mathbf{a}'}$ since the displacements $\tilde{\mathbf{u}}^i_{\mathbf{b}'}$ can easily be calculated for a given pose $\mathbf{X}$ using $\Delta\mathbf{b}'_i = \mathbf{p} + \mathbf{R}\mathbf{b}'_i - \mathbf{p}^0 + \mathbf{R}^0\mathbf{b}'_i$. The static equilibrium condition of the mobile platform can thus be written as a system of 6 equations for the 6 unknowns $\Delta\rho_i$ considering equation (19).

The inverse kinematic of the stiffness model can thus be calculated using an optimization function that aims to minimize equation (19) through changes of the variables $\Delta\rho_i$. Note that contrary to Dong *et al.* in [10], the global stiffness matrices are not re-evaluated during the optimization process. Even if those matrices depend on the position and orientation of the flexible beams, taking into account those changes in the optimization loop does not increase the final accuracy in our case. Indeed, the small changes of legs orientations over the workspace imply variations of $\Delta\rho_i$ of less magnitude than the measurement noise.

6 EXPERIMENTAL SETUP

Different models of the device are proposed in sections 4 and 5. For each model, different objective functions can be chosen, for sometimes a different number of identifiable parameters. In this section, first an overview of the objective functions that will be used for experimental calibration is given. The set of geometrical parameters of each model is also clearly identified. Then the choice of the photogrammetry process is explained. Finally, in order to increase the robustness of calibration with respect to measurement noise, the measurement configurations are chosen in the telescope workspace through an optimization algorithm.

6.1 Overview

Calibration aims at identifying m model parameters per leg by minimizing an objective function F considering information obtained from N_P measurement configurations.

A common way to perform implicit calibration is to use non-linear least square algorithms that aim at minimizing distance equations. The objective function F can thus be written $F = \sum_{n=1}^{N_P} \mathbf{f}_n^T \mathbf{f}_n$, with $\mathbf{f}_n$ the objective function of the n^{th} measurement configuration.

In parallel robotics, because of the devices kinematic structures, kinematic calibration can often be performed considering each leg independently. In such cases, the objective function F_i can be written for each leg i as $F_i = \sum_{n=1}^{N_P} \mathbf{f}_{i,n}^T \mathbf{f}_{i,n}$, $\mathbf{f}_{i,n}$ being the objective function for the i^{th} leg in the n^{th} measurement configuration.

In this section the objective functions $\mathbf{f}_n$ or $\mathbf{f}_{i,n}$ and the set of model parameters are given for all models presented in this report. At the end of this section, table 2 resumes the different objective functions. In this table, as for all this section, every parameter that have the n subscript is a measurement or is at least issued from measurements of the n^{th} configuration.

6.1.1 6-PUS model

The objective function ${}^1f_{i,n}$ is directly extracted from the kinematic closed-loop equation of section 4.1. Each leg i can be calibrated separately and the set of parameters $\{\mathbf{a}_i^T, \mathbf{b}_i^T, \mathbf{u}_i^T, l_i\}$ describes the complete model.

$$ {}^1f_{i,n} = l_i - \|\mathbf{p}^n + \mathbf{R}^n \mathbf{b}_i^* - \mathbf{a}_i - \rho_i^n \mathbf{u}_i\| \tag{30} $$

6.1.2 Jacobian-based model

Since the i^{th} row of the inverse Jacobian matrix $\mathbf{J}_0^{-1}$ also depends on the initial orientation $\mathbf{R}^0$ of the mobile platform, the calibration can not be performed for each leg separately. The set of parameters is set to $\{\mathbf{a}_i^T, \mathbf{b}_i^T, \mathbf{u}_i^T, l_i, \rho_i^0\}$ for each leg, $\mathbf{X}^0$ being derived from $\boldsymbol{\rho}^0$ through the direct kinematic model of the 6-PUS model.

$$ {}^2\mathbf{f}_n = \boldsymbol{\rho}^n - \boldsymbol{\rho}^0 + \mathbf{J}_0^{-1}(\mathbf{X}^n - \mathbf{X}^0) \tag{31} $$

6.1.3 Beam theory-based model

The objective function is derived from the kinematic closed-loop of leg i of equation (14). Since Δl_{Ai}^n and Δl_{Bi}^n are functions of measurements and design parameters β_i and l_{bi}, the design parameters are $\{\mathbf{a}_i^T, \mathbf{b}_i^T, \mathbf{u}_i^T, l_i, \beta_i, l_{bi}\}$ for each leg i.

$$ {}^3f_{i,n} = (l_i - l_{bi} + \Delta l_{Ai}^n + \Delta l_{Bi}^n) - \|\mathbf{p}^n + \mathbf{R}^n \mathbf{b}_i^* - \mathbf{a}_i - \rho_i^n \mathbf{u}_i\| \tag{32} $$

6.1.4 Stiffness model

The stiffness model considers the static equilibrium of the mobile platform. Thus calibration can not be performed for each leg separately. For each leg i, the geometrical parameters are $\{\mathbf{a}_i^T, \mathbf{b}_i^T, \mathbf{u}_i^T, l_i, l_{bi}\}$. The stiffness parameters $\{k_1^d, k_2^d, k_3^d, k_1^l, k_2^l, k_3^l\}$ which describe the stiffness matrices of a flexure joint and of a leg respectively are assumed to be the same for each leg i.

$$ {}^4\mathbf{f}_n = \tilde{\mathbf{P}}_E + \sum_{i=1}^{6} \mathbf{M}_i^n \tilde{\mathbf{P}}_{\mathbf{b}'}^{i,n} \tag{33} $$

The objective functions of each model are summarized in table 2 below.

n°	Model	Objective function
1	6-PUS	${}^1f_{i,n} = l_i - \|\mathbf{p}^n + \mathbf{R}^n\mathbf{b}_i^* - \mathbf{a}_i - \rho_i^n\mathbf{u}_i\|$
2	Jacobian	${}^2\mathbf{f}_n = \boldsymbol{\rho}^n - \boldsymbol{\rho}^0 + \mathbf{J}_0^{-1}(\mathbf{X}^n - \mathbf{X}^0)$
3	Beam-theory	${}^3f_{i,n} = (l_i - l_{bi} + \Delta l_{Ai}^n + \Delta l_{Bi}^n) - \|\mathbf{p}^n + \mathbf{R}^n\mathbf{b}_i^* - \mathbf{a}_i - \rho_i^n\mathbf{u}_i\|$
4	Stiffness	${}^4\mathbf{f}_n = \tilde{\mathbf{P}}_E + \sum_{i=1}^{6} \mathbf{M}_i^n \tilde{\mathbf{P}}_{\mathbf{b}'}^{i,n}$

Table 2: Objective functions used for calibration

6.2 Photogrammetry process choice

Photogrammetry is chosen as measurement system because of its high accuracy (3 μm of standard deviation) over a wide number of object points. Thus, a final accuracy of some micrometers can be reached after calibration. In order to minimize the influence of non-geometric parameters not considered in the telescope modelling [32], the photogrammetry process will be performed in a clean room under controlled pressure, temperature and humidity conditions.

However, the desired accuracy of 10 μm is only three times the standard deviation of the photogrammetry process. Thus the sensitivity of the calibration results to measurement noise has to be set to its minimum. This can be done through a proper choice of the measurement configurations as explained in section 6.3.

6.3 Measurement configurations

The last step of the calibration setup is to define the measurement configurations. It was shown that a proper choice of the measurement configurations increase the robustness of calibration with respect to measurement noise [33]. Algorithms of configuration choice are always based on observability indices [34, 35], based on properties of the observability Jacobian matrix $\mathbf{J}_P$ [36].

To perform the measurement configuration choice, we choose to consider the observability index O_1, the determinant of $\mathbf{J}_P^T\mathbf{J}_P$, since it considers all the singular values of $\mathbf{J}_P^T\mathbf{J}_P$ which allows to obtain an optimum over a reasonable computation time.

The structure of the used algorithm is presented in figure 13, where X_n stands for one configuration of measurement with $n = 1 \dots N_P$, with N_P the total number of measurement configurations for calibration and W the workspace of the telescope.

Find $\mathbf{X}_{opt} = \{X_1, \ldots, X_{N_P}\}$
such as **Max** $\det\left(\mathbf{J}_P^T(\mathbf{X})\mathbf{J}_P(\mathbf{X})\right)$
with respect to $X_n \in W$, for $n = 1...N_P$

Figure 13: Algorithm of the measurement configurations choice

6.3.1 Observability matrix

The measurement configuration choice is performed considering the telescope as a perfect 6-PUS, with objective function ${}^1f_{i,n}$ of equation (30). Simulations of calibration show that parameters a_i^z, b_i^z and l_i are linearly related in the equations and thus cannot be both identifiable. Indeed, differentiating ${}^1f_{i,n}$ with respect to only a_i^z, b_i^z and l_i leads to the observability matrix $\mathbf{J}_P^3$ whose i^{th} row for the n^{th} configuration is given in equation (34):

$$(\mathbf{J}_P^3)_{i,n} = \left[\frac{\mathbf{g}_{i,n}^T}{2\sqrt{\mathbf{g}_{i,n}^T\mathbf{g}_{i,n}}} \begin{bmatrix} 0 & \\ 0 & -\mathbf{z}_E^n \\ 1 & \end{bmatrix}, 1 \right] \tag{34}$$

We have to notice that $\mathbf{g}_{i,n} = \mathbf{p}^n + \mathbf{R}^n\mathbf{b}_i^* - \mathbf{a}_i - \rho_i^n\mathbf{u}_i \approx l_i\mathbf{z}_i^n$. Thus ${}^1f_{i,n}$ can be rewritten considering the parameters uncertainties δa_i^z, δb_i^z and δl_i as:

$$2({}^1f_{i,n}) = (\mathbf{z}_i^n)^T\mathbf{z}_0\delta a_i^z - (\mathbf{z}_i^n)^T\mathbf{z}_E^n\delta b_i^z + \delta l_i \tag{35}$$

Because of the small orientation workspace of the telescope, $\mathbf{z}_E^n$ does not vary too much and is almost equal to $\mathbf{z}_0$ considering the measurement noise. Moreover, the legs cannot be bent at an angle more than 0.6°, which implies that $\mathbf{z}_i^n$ has only small variations: $(\mathbf{z}_i^n)^T\mathbf{z}_0 \approx \lambda$, with λ a constant. Thus equation (35) can be rewritten as:

$$2({}^1f_{i,n}) = \lambda\delta a_i^z - \lambda\delta b_i^z + \delta l_i \tag{36}$$

It is now clear from equation (36) that a_i^z, b_i^z and l_i are linearly related in the equations of calibration. Thus among those three parameters only one can be identified. Considering the assembly and manufacturing tolerances, it was found that l_i supports the maximal uncertainties among those three parameters. Thus, we choose to identify l_i. Note that $\mathbf{u}_i$ is a unit vector and thus can be fully described by only two of its components u_i^x and u_i^y. The set of identifiable parameters is consequently reduced to $\{a_i^x, a_i^y, b_i^x, b_i^y, u_i^x, u_i^y, l_i\}$ for each leg i. Differentiating ${}^1f_{i,n}$ with respect to the 7 identifiable parameters gives the observability Jacobian matrix $\mathbf{J}_P$. The i^{th} row of $\mathbf{J}_P$ for the n^{th} configuration is given in equation (37):

$$(\mathbf{J}_P)_{i,n} = \left[\frac{\mathbf{g}_{i,n}^T}{2\sqrt{\mathbf{g}_{i,n}^T\mathbf{g}_{i,n}}} \begin{bmatrix} 1 & 0 & & & \rho_i^n & 0 \\ 0 & 1 & -\mathbf{x}_E^n & -\mathbf{y}_E^n & 0 & \rho_i^n \\ 0 & 0 & & & 0 & 0 \end{bmatrix}, 1 \right] \tag{37}$$

6.3.2 Algorithm validation

In order to validate results of the algorithm presented in figure 13, a comparison between three different algorithms of measurement configurations choice is performed through simulations of calibration.

The first algorithm choose N_P random configurations in the device workspace and is used as a reference. The second one is the IOOPS (refer to [33] for details) which considers an initial set of calibration poses and then eliminates and adds poses for maximizing O_1. The third one

is the algorithm of figure 13 which directly optimizes the entire set of poses using the *fmincon* function of MATLAB.

The comparison is performed regarding the final accuracy reached after calibration. First, an ideal 6-PUS with exact geometric parameters is considered. Then initial guesses of the geometrical parameters are obtained by adding random uncertainties with a normal distribution of variance 0.5 mm to the exact parameters. For each considered measurement configuration, the exact parameters are used to calculate the position and orientation of the mobile platform, and a measurement noise of variance 2 μm is then added. Finally, implicit calibration is performed considering the N_P measurement configurations.

Results are given in figure 14. For each number of calibration poses N_P, each algorithm is repeated 17 times. The mean and the standard deviation of the obtained positioning accuracy for the 17 configuration sets are represented as an error bar.

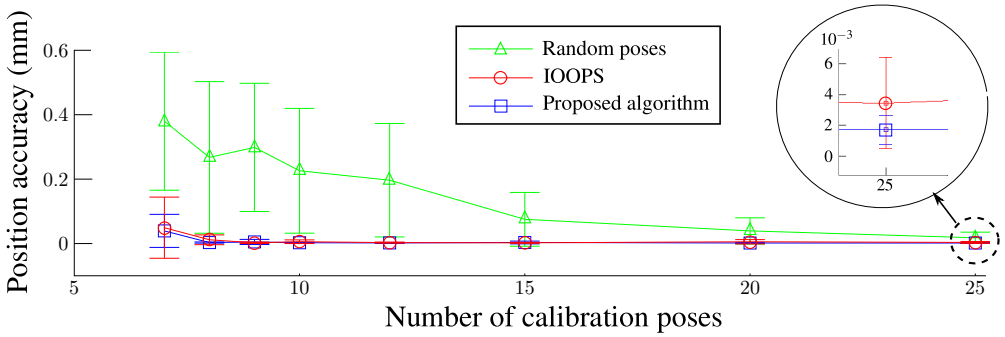

Figure 14: Comparison between algorithms of poses choice

Figure 14 validates the proposed algorithm of figure 13 since it allows to obtain the best accuracy results after calibration. However, its computation time is about five times higher to the IOOPS algorithm that performs only "local" optimizations. With both the IOOPS and the proposed algorithm, optimal configurations are found to be at or very close to the boundary of the telescope workspace.

6.3.3 Results

Algorithm of figure 13 is used to find the N_P optimal measurement configurations for calibration. Even if those configurations are optimal for calibration of a 6-PUS, they will also be used for calibration of the other models of section 4 and 5. Indeed, considering the same measurement configurations for all models allows to compare results of calibration while reducing the total number of measurements. Moreover, the identification of the model parameters of the joints depends on the bending of the flexure joints, and the maximal bending of the flexure joints is obtained when the telescope is at its workspace boundary. Since the optimal configurations are found to be at or very close to the boundary of the telescope workspace, we made the assumption that the optimal configuration poses for a 6-PUS allow calibration of more complete models of the flexure joints. Considering the stiffness model, 10 parameters per leg and 6 stiffness parameters can be identified. Thus, if the position and orientation of the platform are extracted from the photogrammetry data, at least 12 measurement configurations are needed. For safety reasons, we choose to perform calibration on $N_P = 40$ poses. Results of the optimization algorithm for the 40 measurement configurations are shown on table 3, with $\Delta\rho_i$ the maximum range of the i^{th} actuator. For verification purpose, 6 verification poses are also considered.

n°	1	2	3	4	5	6	7	8	9	10
$\Delta\rho_1$	1	1	0	1	1	0	1	1	−1	−1
$\Delta\rho_2$	−1	0	1	1	1	0	1	−1	−1	1
$\Delta\rho_3$	−1	1	−1	0	1	−1	0	−1	−1	−1
$\Delta\rho_4$	1	1	−1	−1	0	−1	0	0	0	0
$\Delta\rho_5$	1	1	0	−1	−1	1	0	−1	−1	−1
$\Delta\rho_6$	−1	−1	1	1	1	1	−1	−1	−1	−1
n°	11	12	13	14	15	16	17	18	19	20
$\Delta\rho_1$	−1	1	−1	1	−1	−1	1	−1	0	−1
$\Delta\rho_2$	−1	−1	1	1	−1	0	1	−1	−1	1
$\Delta\rho_3$	−1	0	−1	0	0	1	1	1	1	1
$\Delta\rho_4$	1	1	−1	0	−1	−1	1	0	−1	0
$\Delta\rho_5$	−1	1	1	0	0	1	−1	−1	1	−1
$\Delta\rho_6$	0	−1	−1	−1	−1	1	0	−1	−1	−1
n°	21	22	23	24	25	26	27	28	29	30
$\Delta\rho_1$	1	−1	1	0	1	−1	−1	−1	−1	1
$\Delta\rho_2$	−1	−1	1	−1	−1	1	1	1	1	−1
$\Delta\rho_3$	0	0	1	1	−1	1	−1	1	1	0
$\Delta\rho_4$	1	0	−1	−1	1	0	−1	0	−1	−1
$\Delta\rho_5$	1	1	−1	0	1	−1	1	−1	0	1
$\Delta\rho_6$	1	1	−1	1	1	0	1	−1	1	1
n°	31	32	33	34	35	36	37	38	39	40
$\Delta\rho_1$	1	0	1	−1	−1	0	1	1	−1	1
$\Delta\rho_2$	1	1	1	1	1	0	0	1	0	−1
$\Delta\rho_3$	0	−1	1	−1	0	1	−1	0	1	−1
$\Delta\rho_4$	−1	−1	−1	1	1	−1	1	1	−1	−1
$\Delta\rho_5$	0	−1	−1	−1	1	−1	1	1	−1	−1
$\Delta\rho_6$	1	1	0	−1	0	−1	1	−1	−1	1

Table 3: 40 optimized measurement configurations

n°	1	2	3	4	5	6
$\Delta\rho_1$	−0.5	0.5	0.5	−0.5	0.5	−0.5
$\Delta\rho_2$	0	1	0	0.5	1	0
$\Delta\rho_3$	−1	0	0	−1.0	−0.5	0
$\Delta\rho_4$	0	1	0	0.5	0.5	1
$\Delta\rho_5$	0	1	1	0	1	0.5
$\Delta\rho_6$	−0.5	0.5	−0.5	0	0.5	0

Table 4: 6 verification configurations

7 EXPERIMENTAL RESULTS

This section gives the experimental results of calibration of the space telescope using photogrammetry data. For each measurement configuration, the position and orientation of the mobile platform are extracted from the photogrammetry object points using Haralick method. Calibration minimizes each objective function of section 6.1 without considering the mobile platform deformation, with the linear model and with the matrix model respectively. The accuracy reached after calibration is compared for all models in section 7.4, which allows the choice of the most suitable model for the telescope.

Every calibration is performed considering the objective functions presented in section 6.1 and utilizes the *lsqnonlin* function of MATLAB. Same results are obtained utilizing either the Levenberg-Marquardt or the trust-region reflective algorithms. Experiments showed that in our case, those algorithms are non sensitive to changes on the initial parameters.

7.1 Without considering the mobile platform deformation

For all this section, the mobile platform deformation is not taken into account for comparison purpose. Thus in all the objective functions of section 6.1, the following relation is considered: $\mathbf{b}_i^* = \mathbf{b}_i$.

For the kinematic and stiffness models, first the parameter identifiability is analysed and calibration results are given as distances between nominal and identified values of the model parameters in table 5. Then, results of final positioning and orientation accuracies are given in figure 15.

7.1.1 with the 6-PUS model

The experimental calibration confirms that only one parameter among $\{a_i^z, b_i^z, l_i\}$ can be identified. Regarding the actuator orientation $\mathbf{u}_i$, only one of its components can be experimentally identified, whatever the used parametrization. We choose to identify u_i^x while setting u_i^y to zero. Thanks to the knowledge of those two components, u_i^z can be easily calculated since $\mathbf{u}_i$ is a unit vector. Note that the choice of which component of $\mathbf{u}_i$ is identified does not change the experimental calibration results. The set of identifiable parameters is thus reduced to $\{a_i^x, a_i^y, b_i^x, b_i^y, u_i^x, l_i\}$ while a_i^z, b_i^z and u_i^y are set to zero. Calibration is performed and results are given in table 5 as distances between the parameter identified values and their nominal ones.

7.1.2 with the Jacobian-based model

Since the Jacobian matrix is derived from the 6-PUS model, the same identifiability problems appear. However, since the small device workspace is already considered in the definition of the Jacobian-based model, explanations of the non-identifiable parameters can be directly given from the shape analyse of the Jacobian matrix. Indeed, each row of the Jacobian matrix only takes into account the leg orientation $\mathbf{z}_i^0$, the position of point $\mathbf{b}_i^*$ and the scalar product $\mathbf{u}_i^T\mathbf{z}_i^0$ between the actuator and leg orientations of the initial pose $\mathbf{X}^0$ of the device. Thus for each leg, if $\mathbf{b}_i^*$ is known, only a_i^x and a_i^y can be identified considering the initial legs orientation $\mathbf{z}_i^0$. Then, only one more information is not yet utilized which is the scalar product $\mathbf{u}_i^T\mathbf{z}_i^0$. So only one component of $\mathbf{u}_i$ can be identified.

Since b_i^z and l_i are linearly related, we choose to identify l_i instead of b_i^z for comparison purpose with other models. Moreover, the same conclusion on the parametrization of $\mathbf{u}_i$ was observed: changing its parametrization does not influence the calibration results. As for the

initial position $\boldsymbol{\rho}_0$ of the actuators, first their identification do not change the final accuracy reach after calibration, and then, they are found to be low-observable. Indeed, identifying $\boldsymbol{\rho}_0$ leads to 6 singular values of $\mathbf{J}_P^T\mathbf{J}_P$ being under 10^{-14}. On the other hand, when $\boldsymbol{\rho}_0$ are not identified, the smallest singular value of $\mathbf{J}_P^T\mathbf{J}_P$ is 10^{-4}. Thus, considering the measurement noise, it is preferable to not identify $\boldsymbol{\rho}_0$. So the identifiable parameters are setted to $\{a_i^x, a_i^y, b_i^x, b_i^y, u_i^x, l_i\}$ for each leg i.

7.1.3 with the beam theory-based model

Because of the small joints orientation $\delta \leq 1°$, variations of Δl_{Ai} and Δl_{Bi} are less than 0.3 μm. Considering a measurement noise of 5 μm on the object points, it is clear that Δl_{Ai} and Δl_{Bi} can not be properly identified. Thus the identified parameters are still the same as the 6-PUS model and β_i and l_{bi} are fixed to their nominal values.

7.1.4 with the stiffness model

The stiffness equation considers the loads $\tilde{\mathbf{P}}^i_{\mathbf{b}'}$ acting on points $\mathbf{b}'_i$. Those loads are functions of the displacements $\tilde{\mathbf{u}}^i_{\mathbf{a}'}$ and $\tilde{\mathbf{u}}^i_{\mathbf{b}'}$ as shown in equation (29). Points $\mathbf{b}'_i$ and $\mathbf{a}'_i$ being functions of $\mathbf{b}_i$ and $(\mathbf{a}_i + \rho_i\mathbf{u}_i)$ respectively, the positions of $\mathbf{b}_i$ and $\mathbf{a}_i$ can be thought to be identifiable. However, since a_i^z, b_i^z and l_i are linearly related, only l_i will be identified. The extra information in $(\mathbf{a}_i + \rho_i\mathbf{u}_i)$ will be used to identify u_i^x.

The stiffness model also considers stiffness parameters. However, experiment shows that none of them can be properly identified. Hence, the set of identifiable parameters for each leg becomes $\{a_i^x, a_i^y, b_i^x, b_i^y, u_i^x, l_i\}$.

7.1.5 Results

For both the models, the calibration results are given as distances between the nominal and identified parameter values in table 5. Experimental results are also given in term of final accuracy for each identified model in figure 15. The position error refers to the distance between the calculated and the measured position of the center of the mobile platform. The orientation error is the angle of the axis-angle representation between the calculated and the measured orientation of the mobile frame $\mathcal{F}_E$. Each bar has the size of the maximal error and the additional line stands for the average error. For the verification poses, the mean and maximal values are provided.

Figure 15 shows that the same final positioning accuracy can be reached for both models. As for the orientation accuracy, better results are obtained while not considering the static equilibrium of the mobile platform. Thanks to the small workspace of the telescope, the Jacobian-based model gives similar results as the 6-PUS model. Moreover, considering the parasitic shift of the flexure joints over this small workspace does not improve the accuracy results since their deflections are less than 0.3 μm with the beam theory-based model.

However, as shown in table 5, the identified values of the model parameters are quite "far" from their nominal values, which does not correspond to the manufacturing tolerances. The most important deviations are obtained in the identification of u_x for both the models. Those deviations can be explained regarding the linear model of the mobile platform deformation as done in section 7.2.

i	1	2	3	4	5	6
Δa_i^x	0.98	−0.23	−2.72	−2.31	0.37	4.42
Δa_i^y	2.62	2.57	−2.55	−1.97	−1.76	−2.42
Δb_i^x	3.59	0.73	−0.09	2.45	−3.67	−0.49
Δb_i^y	−1.38	−0.88	4.22	1.39	−0.02	3.04
Δu_i^x	−0.07	0.05	0.10	−0.06	0.05	−0.15
Δl_i	0.95	0.07	1.53	0.50	0.63	1.22

(a) For the 6-PUS model

i	1	2	3	4	5	6
Δa_i^x	1.33	0.09	−2.46	−3.32	0.90	3.31
Δa_i^y	3.25	3.36	−2.18	−2.40	−2.56	−2.53
Δb_i^x	3.75	0.48	−0.85	1.79	−3.15	0.13
Δb_i^y	−0.79	−0.08	5.35	2.38	−0.26	2.73
Δu_i^x	−0.09	0.07	0.12	−0.07	0.07	−0.17
Δl_i	0.95	0.24	1.78	0.38	0.58	1.29

(b) For the Jacobian-based model

i	1	2	3	4	5	6
Δa_i^x	0.99	−0.25	−2.73	−2.31	0.36	4.43
Δa_i^y	2.60	2.57	−2.57	−1.98	−1.78	−2.44
Δb_i^x	3.58	0.73	−0.09	2.45	−3.66	−0.50
Δb_i^y	−1.36	−0.86	4.25	1.41	0.00	3.06
Δu_i^x	−0.07	0.05	0.10	−0.06	0.05	−0.15
Δl_i	0.94	0.06	1.54	0.50	0.62	1.23

(c) For the beam theory-based model

i	1	2	3	4	5	6
Δa_i^x	−0.40	0.22	0.87	−2.64	0.55	4.18
Δa_i^y	2.14	2.45	−2.73	−0.20	0.29	−2.97
Δb_i^x	3.05	0.14	1.46	4.02	−4.85	0.31
Δb_i^y	−2.72	−1.23	5.91	3.57	0.50	3.95
Δu_i^x	−0.05	0.05	−0.05	−0.02	0.03	−0.17
Δl_i	1.15	0.31	1.95	0.68	1.05	1.64

(d) For the stiffness model

Table 5: Distances between nominal and identified parameter values for the fourth considered models without considering the mobile platform deformation (in mm)

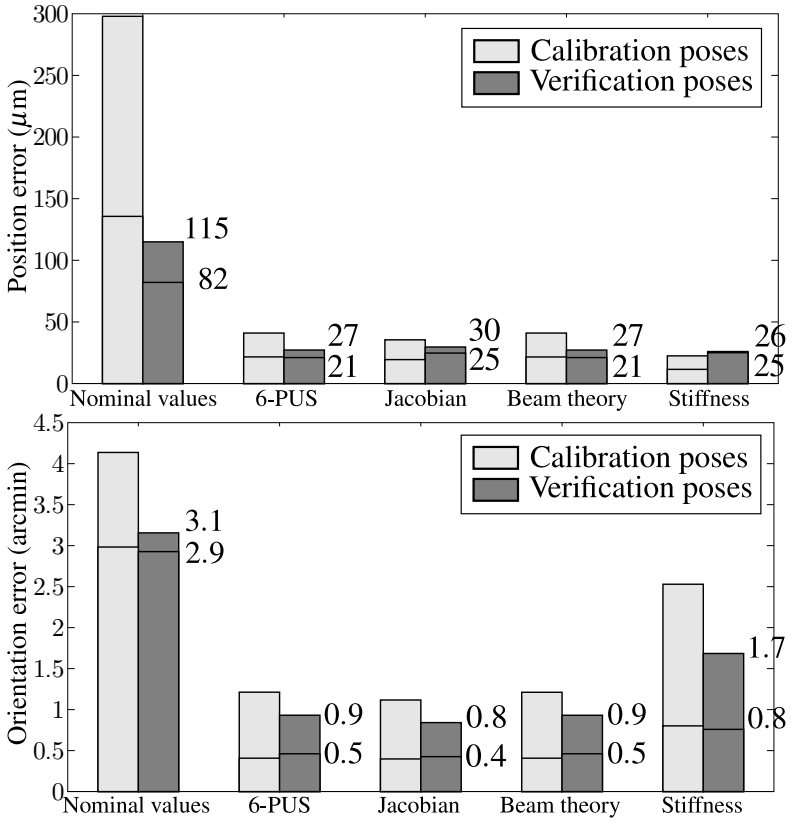

Figure 15: Positioning and orientation errors on calibration and verification poses for the 4 models without considering the mobile platform deformation, the average and maximal errors are provided for the verification poses

7.2 With the linear model of the mobile platform deformation

In this section, the linear model for the mobile platform deformation is taken into account. Thus, the following relation is considered: $\mathbf{b}_i^* = \mathbf{b}_i + \kappa_i \Delta\rho_i \mathbf{z}_o$.

For both models, the identifiability of the model parameters does not change from section 7.1. However, κ_i also has to be identified for each leg. Experiments show that κ_i and u_i^x cannot be both identified. Indeed, those two parameters are found to be linearly related, as explained below. Let consider the objective function ${}^1f_{i,n}$ of the 6-PUS model with the linear model for the mobile platform deformation:

$$ {}^1f_{i,n} = l_i - \|\mathbf{p}^n + \mathbf{R}^n(\mathbf{b}_i + \kappa_i \Delta\rho_i \mathbf{z}_o) - \mathbf{a}_i - \rho_i^n \mathbf{u}_i\| \tag{38} $$

Because of the small workspace of the telescope, the platform orientation does not vary too much and approximating $\mathbf{R}^n(\kappa_i \Delta\rho_i^n \mathbf{z}_o)$ by $(\kappa_i \Delta\rho_i^n \mathbf{z}_o)$ leads to maximal errors of less than 1 μm for $n = 1...N_p$. Let also consider that $\mathbf{u}_i$ is set to its nominal value $\mathbf{z}_o$, then equation (38) can be rewritten as:

$$ f_{i,n} = l_i - \|\mathbf{p}^n + \mathbf{R}^n \mathbf{b}_i - \mathbf{a}_i - (\rho_i^n - \kappa_i \Delta\rho_i^n)\mathbf{u}_i\| \tag{39} $$

Considering $\rho_i^n = \rho_i^0 + \Delta\rho_i^n$ leads to:

$$ f_{i,n} = l_i - \|\mathbf{p}^n + \mathbf{R}^n \mathbf{b}_i - \mathbf{a}_i - \rho_i^0 \mathbf{u}_i - (1 - \kappa_i)\Delta\rho_i^n \mathbf{u}_i\| \tag{40} $$

Analysing the term $(1 - \kappa_i)\Delta\rho_i^n \mathbf{u}_i$ shows that when the mobile platform deformation is not considered, the identification of κ_i is accounted in the identification of $\mathbf{u}_i$. This results in values of u_i^x being far from their nominal values as shown on table 5. This also explains why only one component of $\mathbf{u}_i$ can be identified while not considering the mobile platform deformation. Indeed, the identification process automatically considers the platform deformation in a linear approximation and distributes the model errors on the parameter identification. Since the linear approximation is only one degree of freedom, only one component of $\mathbf{u}_i$ can be identified.

Thus, in order to take into account the mobile platform deformation, κ_i will be identified for both models while setting $\mathbf{u}_i$ to its nominal value $\mathbf{z}_o$. Moreover, setting $\mathbf{u}_i$ to its nominal value allows us to consider the mobile platform deformation directly in the actuator positions ρ_i such as: $\rho_i = \rho_i^0 + (1 - \kappa_i)\Delta\rho_i$. Results are provided in table 6 and figure 16.

For both models, it is interesting to note that the same accuracy results are obtained considering or not the mobile platform deformation in a linear model. This is due to the calibration that accounts the mobile platform deformation in the parameter identification. Indeed, instead of identifying κ_i, the linear model of the mobile platform deformation is automatically taken into account in the identification of u_i^x as explained above. As for the identified values of the other model parameters, they are quite the same comparing tables 5 and 6, which is as expected since the mobile platform deformation is considered in a linear model in both cases. However, their identified values stay quite "far" from their *a priori*. Considering the matrix model in section 7.3, we will see that those deviations are not only due to geometric uncertainties but mainly due to the mobile platform deformation that is accounted in the parameter identification.

i	1	2	3	4	5	6
Δa_i^x	0.32	0.29	−1.74	−2.93	0.89	2.95
Δa_i^y	2.66	2.60	−2.54	−1.99	−1.71	−2.40
Δb_i^x	3.59	0.72	−0.09	2.43	−3.72	−0.44
Δb_i^y	−1.34	−0.87	4.24	1.40	0.01	3.02
Δl_i	0.91	0.05	1.48	0.48	0.62	1.11
$10^3\Delta\kappa_i$	7.10	1.60	−0.61	1.62	−0.72	6.48

(a) For the 6-PUS model

i	1	2	3	4	5	6
Δa_i^x	1.43	−0.01	−2.57	−3.33	0.93	3.42
Δa_i^y	3.30	3.45	−2.15	−2.48	−2.63	−2.51
Δb_i^x	3.79	0.44	−0.94	1.74	−3.10	0.22
Δb_i^y	−0.68	0.04	5.33	2.34	−0.30	2.69
Δl_i	0.70	0.03	1.64	0.19	0.41	1.05
$10^3\Delta\kappa_i$	13.14	7.94	3.10	5.37	4.47	11.57

(b) For the Jacobian-based model

i	1	2	3	4	5	6
Δa_i^x	0.32	0.28	−1.74	−2.93	0.88	2.95
Δa_i^y	2.65	2.59	−2.55	−2.00	−1.73	−2.42
Δb_i^x	3.59	0.71	−0.09	2.43	−3.72	−0.43
Δb_i^y	−1.32	−0.84	4.26	1.42	0.04	3.04
Δl_i	0.91	0.05	1.49	0.47	0.61	1.12
$10^3\Delta\kappa_i$	7.11	1.64	−0.60	1.63	−0.69	6.51

(c) For the beam theory-based model

i	1	2	3	4	5	6
Δa_i^x	−0.91	0.75	0.60	−2.83	0.84	2.63
Δa_i^y	2.16	2.47	−2.78	−0.21	0.26	−2.92
Δb_i^x	3.03	0.13	1.61	4.03	−4.83	0.44
Δb_i^y	−2.74	−1.18	5.91	3.60	0.46	3.98
Δl_i	1.13	0.29	1.95	0.67	1.04	1.50
$10^3\Delta\kappa_i$	2.61	2.01	−13.57	−7.48	−5.58	11.65

(d) For the stiffness model

Table 6: Distances between nominal and identified parameter values for the fourth models considering the linear model of the mobile platform deformation (in mm except for $\Delta\kappa_i$ which is dimensionless)

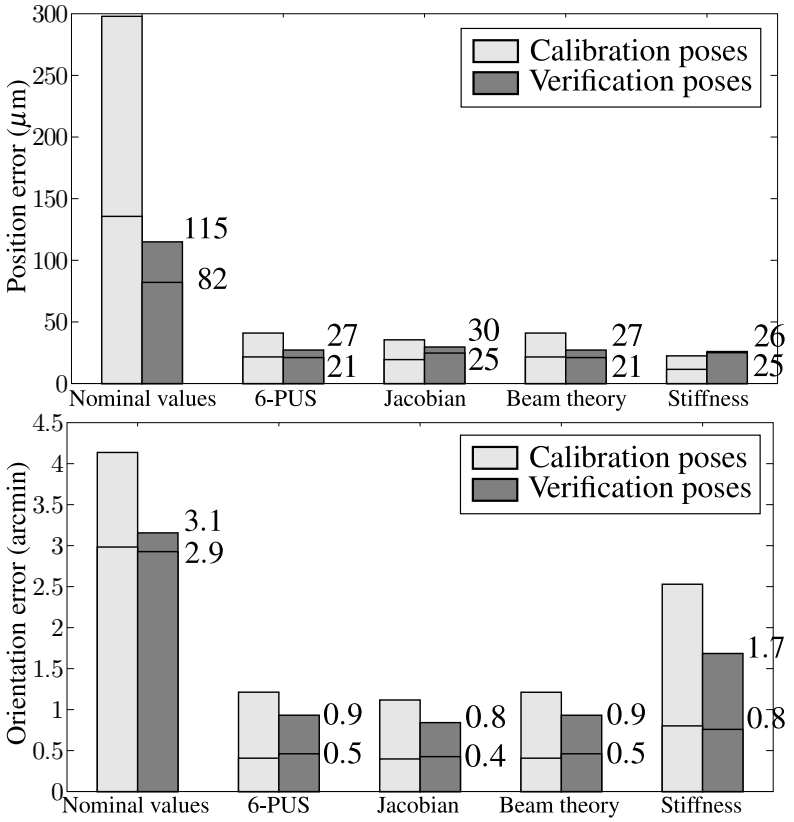

Figure 16: Positioning and orientation errors on calibration and verification poses for the 4 models with the linear model of the mobile platform deformation, the average and maximal errors are provided for the verification poses

7.3 With the matrix model of the mobile platform deformation

In this section the matrix model of deformation is taken into account. Thus, the following relation is considered: $\mathbf{b}_i^* = \mathbf{b}_i + (\mathbf{k}_i \Delta\boldsymbol{\rho})\mathbf{z}_o$, with $\mathbf{k}_i$ the i^{th} row of the coefficient matrix $\mathbf{K}$.

As for the linear model, $\mathbf{k}_i$ and u_i^x cannot be both identified. Moreover, setting u_i^x to its nominal value allows the identification of only one term in $\mathbf{k}_i$. Experiments show that the best accuracy results are obtained by identifying all the diagonal terms of $\mathbf{K}$, which actually relate to the coefficients κ_i of the linear model. The diagonal terms of matrix $\mathbf{K}$ are identified and are referred as κ_i in table 7.

The final accuracy reached after calibration is given in figure 17. It shows that a better orientation accuracy is obtained considering the matrix model for the mobile platform deformation. However, regarding the telescope requirements, the desired orientation accuracy of 180 arcmin is already reached by the linear model. Moreover, no significant improvement on the positioning accuracy are observed for the matrix model. Since the matrix model needs information on the mobile platform deformation in order to identify the coefficient matrix $\mathbf{K}$ and since our objective is to find the most suitable model to calibrate the telescope in space with only measurements of the position and orientation of the mobile platform, the linear model of deformation will be preferred.

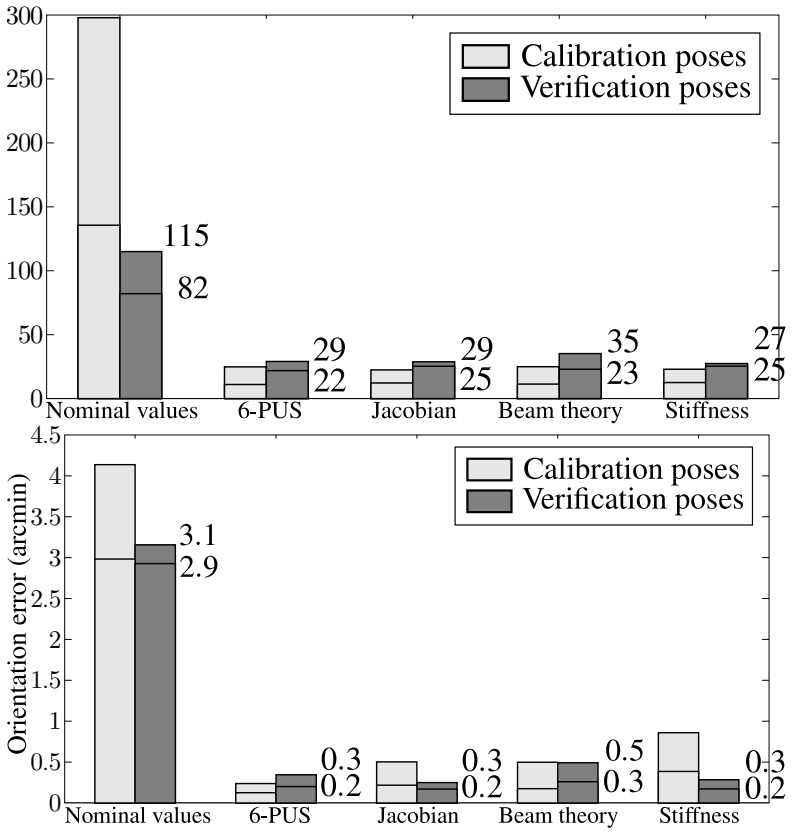

Figure 17: Positioning and orientation errors on calibration and verification poses for the 4 models with the matrix model of the mobile platform deformation, the average and maximal errors are provided for the verification poses

i	1	2	3	4	5	6
Δa_i^x	−1.71	0.41	0.30	−1.58	−0.18	−0.34
Δa_i^y	−0.33	−0.21	−2.12	0.37	0.98	−2.62
Δb_i^x	0.56	1.91	0.04	0.41	−1.82	−0.32
Δb_i^y	−0.19	−0.21	2.25	1.46	0.61	−0.22
Δl_i	0.37	−0.45	1.02	0.25	0.43	0.58
$10^3\Delta\kappa_i$	9.58	1.98	4.43	3.33	0.67	6.99

(a) For the 6-PUS model

i	1	2	3	4	5	6
Δa_i^x	−0.58	0.11	−0.52	−1.99	−0.13	0.15
Δa_i^y	0.34	0.63	−1.72	−0.11	0.06	−2.70
Δb_i^x	0.77	1.64	−0.82	−0.26	−1.20	0.36
Δb_i^y	0.48	0.70	3.34	2.41	0.30	−0.53
Δl_i	0.16	−0.47	1.17	−0.04	0.23	0.52
$10^3\Delta\kappa_i$	15.77	8.25	8.16	7.02	5.93	12.13

(b) For the Jacobian-based model

i	1	2	3	4	5	6
Δa_i^x	−2.77	0.62	0.94	−1.50	−0.18	−1.30
Δa_i^y	−1.13	−0.42	−2.37	0.83	1.02	−2.88
Δb_i^x	0.21	1.98	0.53	0.74	−1.87	−1.16
Δb_i^y	−1.39	−0.42	2.38	1.77	0.70	0.11
Δl_i	0.56	−0.42	1.12	0.31	0.43	0.72
$10^3\Delta\kappa_i$	1.03	0.14	0.51	0.59	0.50	0.81

(c) For the beam theory-based model

i	1	2	3	4	5	6
Δa_i^x	−0.82	−0.72	0.93	−1.64	−0.00	1.63
Δa_i^y	1.08	0.19	−1.49	−0.46	0.69	−2.74
Δb_i^x	0.49	1.41	0.06	0.38	−0.83	2.15
Δb_i^y	0.98	1.30	3.07	2.13	0.45	−0.37
Δl_i	0.17	−0.68	1.08	0.00	0.26	0.58
$10^3\Delta\kappa_i$	15.89	12.00	0.53	3.90	6.91	21.19

(d) For the stiffness model

Table 7: Distances between nominal and identified parameter values for the fourth models considering the matrix model of the mobile platform deformation (in mm except for $\Delta\kappa_i$ which is dimensionless)

7.4 Results analysis

With or without considering the mobile platform deformation, the Jacobian-based, the beam theory-based and the stiffness models give similar accuracy results as the 6-PUS model. This is due to the small workspace of the telescope. Indeed, because of the small orientation of the flexure joints over the entire workspace, their parasitic shift stay negligible and their generated stresses do not influence the mobile platform positioning. Thus they can be modelled by pure spherical joints as it is done in the 6-PUS model.

Regarding the developed models of deformation, both of them give quite the same accuracy results. However, without considering the deformation or with the linear model, the identified model parameters are found to be "far" from their *a priori*. The deviation of u_i^x was already explained in section 7.2. However, the mobile platform deformation is also accounted in the other identified parameters as shown on figure 18. In order to highlight those deviations, errors between the nominal values and the identified parameters are amplified in the figure.

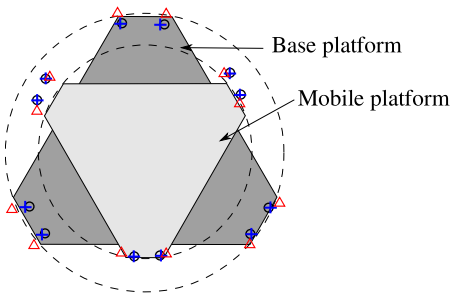

Figure 18: Representation of errors between the nominal and identified parameters values of the 6-PUS model without considering the mobile platform deformation (circle) and with the linear (cross) and the matrix models (triangle) of the mobile platform deformation

Figure 18 shows that the minimum deviations from the nominal parameters are obtained for the points marked by triangles, when the mobile platform deformation is considered with the matrix model. This result is as expected since the matrix model is a good approximation of the mobile platform deformation. Thus, this inaccuracy source does not need to be accounted in the parameter identification, which allows the identified parameters to be closer to their nominal values when considering the matrix approximation.

Without considering the mobile platform deformation or with the linear model, we remark that the identified positions of points $\mathbf{a}_i$ and $\mathbf{b}_i$ do not correspond to the initial design of the telescope. For example, the identified geometry of the base platform considers a smaller design parameter α_0 as its initial design. Those modifications must again be due to the platform deformation: errors that cannot be taken into account in the identification of $\mathbf{u}_i$ are accounted in the other identified parameters.

However, the goal of calibration is to obtain the most suitable accuracy considering the robot requirements. In our case, the positioning accuracy is more critical than the orientation one as regards to the accuracy results, and both the developed models for the mobile platform deformation give similar results for the positioning accuracy. Thus, the choice of the most suitable model of deformation cannot be done regarding the final accuracy. However, our objective is to develop a model of the telescope that will be used for calibration in space. Thus we will only have access to measurements of position and orientation of the mobile platform, which means that the identification of the coefficient matrix $\mathbf{K}$ cannot be made in space. So we made the choice to use the linear model in order to take into account the mobile platform deformation.

8 CONCLUSIONS

The accurate calibration of the active space telescope allows us to choose the most suitable model for the telescope. Two sources of inaccuracy were considered and modelled: the mobile platform deformation and the flexure joints behaviour.

Concerning the behaviour of the flexure joints, the models developed based on equations of the beam theory and those developed considering the static equilibrium of the mobile platform give the same accuracy results as the 6-PUS model. Indeed, because of the small deflection of the flexure joints over the small workspace of the telescope, their parasitic shift, just as the influence of their generated stresses on the mobile platform equilibrium, are negligible. Thus the flexure joints can be modelled by perfect spherical joints.

The mobile platform deformation was considered with two models of deformation. The matrix model seems to be a good approximation of those deformations since it allows the identified model parameters to be close to their nominal values. However, good positioning accuracy results are also obtained either with the linear model or by ignoring the mobile platform deformation. This is due to calibration that accounts for the model errors in the parameter identification. This leads to identified parameter values being "far" from their *a priori*. This report explains that those deviations are not only due to geometric uncertainties on the telescope parameters but mainly due to the platform deformation that is accounted in the parameter identification.

However, it is not always possible to directly use the identified parameter values in the control loop of a robot, namely if calibration is not performed regarding the control requirements. For example, it can be problematic to consider unreal values of the geometric model parameters for dynamic control of a robot. The space telescope only has slow motions over a small workspace, which allows the use of the kinematic Jacobian in the control loop. Thus, having identified parameter values being "far" from their *a priori* does not influence the telescope functioning in our case as long as it allows a good positioning accuracy. So the linear model of the mobile platform deformation can be considered, which enables calibration of the telescope in space where only the position and orientation of the mobile platform can be measured.

ACKNOWLEDGMENT

This work was supported by Thales Alenia Space and the Region "Provence-Alpes-Côte-d'Azur".

References

[1] C. Dumas, S. Caro, S. Garnier, and B. Furet, "Joint stiffness identification of six-revolute industrial serial robots," *Robotics and Computer-Integrated Manufacturing*, vol. 27, no. 4, pp. 881 – 888, 2011.

[2] M. Rognant, E. Courteille, and P. Maurine, "A systematic procedure for the elastodynamic modeling and identification of robot manipulators," *IEEE Trans. on Robotics*, vol. 26, no. 6, pp. 1085 –1093, 2010.

[3] B. W. Mooring and S. S. Padavala, "The effect of kinematic model complexity on manipulator accuracy," in *IEEE Int. Conf. on Robotics and Automation (ICRA)*, vol. 1, Scottsdale, AZ, May 1989, pp. 593 –598.

[4] J. Wang and O. Masory, "On the accuracy of a stewart platform - part i. the effect of manufacturing tolerances," in *IEEE Int. Conf. on Robotics and Automation (ICRA)*, vol. 1, Atlanta, GA, May 1993, pp. 114 –120.

[5] O. Masory, J. Wang, and H. Zhuang, "Kinematic modeling and calibration of a stewart platform," *Advanced Robotics*, vol. 11, no. 5, pp. 519–539, 1997.

[6] S. Zelenika, M. G. Munteanu, and F. D. Bona, "Optimized flexural hinge shapes for microsystems and high-precision applications," *Mechanism and Machine Theory*, vol. 44, no. 10, pp. 1826 – 1839, 2009.

[7] B.-J. Yi, G. B. Chung, H. Y. Na, W. K. Kim, and I. H. Suh, "Design and experiment of a 3-DOF parallel micromechanism utilizing flexure hinges," *IEEE Trans. on Robotics and Automation*, vol. 19, no. 4, pp. 604 – 612, Aug. 2003.

[8] B. H. Kang, J. Wen, N. Dagalakis, and J. Gorman, "Analysis and design of parallel mechanisms with flexure joints," *IEEE Trans. on Robotics*, vol. 4, no. 6, pp. 4097 – 4102, May 2004.

[9] N. Fazenda, E. Lubrano, S. Rossopoulos, and R. Clavel, "Calibration of the 6 DOF high-precision flexure parallel robot "Sigma 6"," in *Parallel Kinematic Machines in Research and Practice*. Chemnitz: Neugebauer Reimund, 2006, pp. 379–398.

[10] W. Dong, Z. Du, and L. Sun, "Conceptional design and kinematics modeling of a wide-range flexure hinge-based parallel manipulator," in *IEEE Int. Conf. on Robotics and Automation (ICRA)*, Barcelona, Spain, Apr. 2005, pp. 4031 – 4036.

[11] L. Cléroux and C. M. Gosselin, "Modeling and identification of non-geometric parameters in semi-flexible parallel robots," in *International Symposium on Robotics and Manufacturing*, vol. 6, Montpellier, May 1996, pp. 115–120.

[12] P. Vischer and R. Clavel, "Kinematic calibration of the parallel delta robot," *Robotica*, vol. 16, pp. 207–218, 1998.

[13] D. Daney, N. Andreff, G. Chabert, and Y. Papegay, "Interval method for calibration of parallel robots : Vision based experiments," *Mechanism and Machine Theory*, vol. 41, pp. 929–944, 2006.

[14] A. J. Patel and K. F. Ehmann, "Calibration of a hexapod machine tool using a redundant leg," *International Journal of Machine Tools and Manufacture*, vol. 40, no. 4, pp. 489–512, Mar. 2000.

[15] Y. Takeda, G. Shen, and H. Funabashi, "A DBB-Based kinematic calibration method for in-parallel actuated mechanisms using a fourier series," *ASME Journal of Mechanical Design*, vol. 126, no. 5, pp. 856–865, 2004.

[16] H. Zhuang and Z. S. Roth, "Method for kinematic calibration of stewart platforms," *Journal of Robotic Systems*, vol. 10, no. 3, pp. 391–405, 1993.

[17] M. Abtahi, H. Pendar, A. Alasty, and G. Vossoughi, "Experimental kinematic calibration of parallel manipulators using a relative position error measurement system," *Robotics and Computer-Integrated Manufacturing*, vol. 26, no. 6, pp. 799 – 804, 2010.

[18] D. Bennett and J. M. Hollerbach, "Autonomous calibration of single-loop closed kinematic chains formed by manipulators with passive endpoint constraints," *IEEE Trans. on Robotics and Automation*, vol. 7, no. 5, pp. 597–606, Oct. 1991.

[19] M. Ikits and J. M. Hollerbach, "Kinematic calibration using a plane constraint," in *IEEE Int. Conf. on Robotics and Automation (ICRA)*, vol. 4, Albuquesrque NM, USA, Apr. 1997, pp. 3191–3196.

[20] W. Khalil and S. Besnard, "Self calibration of stewart-gough parallel robots without extra sensors," *IEEE Trans. on Robotics and Automation*, vol. 15, no. 6, pp. 1116 –1121, Dec. 1999.

[21] C. W. Wampler, J. M. Hollerbach, and T. Arai, "An implicit loop method for kinematic calibration and its application to closed-chain mechanisms," *IEEE Trans. on Robotics and Automation*, vol. 11, no. 5, pp. 710–724, Oct. 1995.

[22] S. Besnard and W. Khalil, "Calibration of parallel robots using two inclinometers," in *IEEE Int. Conf. on Robotics and Automation (ICRA)*, vol. 3, Detroit, MI, 1999, pp. 1758–1763.

[23] D. Daney, "Kinematic calibration of the gough platform," *Robotica*, vol. 21, no. 6, pp. 667–690, 2003.

[24] J.-P. Merlet, *Parallel Robots, 2nd Edition*. Springer, 2006, vol. 128.

[25] ——, "Articulated device, for use in particular in robotics," Patent 5 053 687, 1991.

[26] J.-P. Merlet and C. M. Gosselin, "Nouvelle architecture pour un manipulateur parallele a six degres de liberte," *Mechanism and Machine Theory*, vol. 26, no. 1, pp. 77 – 90, 1991.

[27] S. Henein, P. Spanoudakis, S. Droz, L. I. Myklebust, and E. Onillon, "Flexure pivot for aerospace mechanisms," in *10th European Space Mechanisms and Tribology Symposium*, San Sebastian, Spain, Sep. 2003, pp. 285–288.

[28] G. Chen, X. Liu, and Y. Du, "Elliptical-arc-fillet flexure hinges: Toward a generalized model for commonly used flexure hinges," *ASME Journal of Mechanical Design*, vol. 133, no. 8, p. 081002, 2011.

[29] R. M. Haralick, H. Joo, C.-N. Lee, X. Zhuang, V. G. Vaidya, and M. B. Kim, "Pose estimation from corresponding point data," *IEEE Trans. on Systems, Man and Cybernetics*, vol. 19, no. 6, pp. 1426 –1446, 1989.

[30] W. J. Zhang, J. Zou, L. G. Watson, W. Zhao, G. H. Zong, and S. S. Bi, "The constant-jacobian method for kinematics of a three-DOF planar micro-motion stage," *Journal of Robotic Systems*, vol. 19, no. 2, p. 63–72, 2002.

[31] L. Chevalier, *Mécanique des systèmes et des milieux déformables*, ellipses ed., 2004.

[32] T. Niaritsiry, N. Fazenda, and R. Clavel, "Study of the sources of inaccuracy of a 3 DOF flexure hinge-based parallel manipulator," in *IEEE Int. Conf. on Robotics and Automation (ICRA)*, vol. 4, New Orleans, May 2004, pp. 4091 – 4096.

[33] D. Daney, Y. Papegay, and M. Blaise, "Choosing measurement poses for robot calibration with the local convergence method and tabu search," *International Journal of Robotics Research*, vol. 24, no. 6, pp. 501–518, 2005.

[34] A. Nahvi and J. M. Hollerbach, "The noise amplification index for optimal pose selection in robot calibration," in *IEEE Int. Conf. on Robotics and Automation (ICRA)*, vol. 1, Minneapolis, Minnesota, 1996, pp. 647–654.

[35] Y. Sun and J. M. Hollerbach, "Observability index selection for robot calibration," in *IEEE Int. Conf. on Robotics and Automation (ICRA)*, Pasadena, CA, May 2008, pp. 831–836.

[36] B. Mooring, M. Driels, and Z. Roth, *Fundamentals of Manipulator Calibration*. New York, NY, USA: John Wiley & Sons, Inc., 1991.

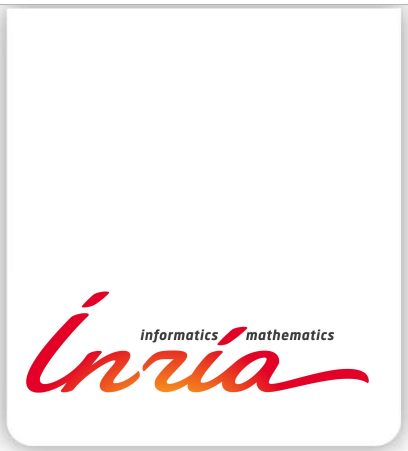

RESEARCH CENTRE
SOPHIA ANTIPOLIS – MÉDITERRANÉE

2004 route des Lucioles - BP 93
06902 Sophia Antipolis Cedex

Publisher
Inria
Domaine de Voluceau - Rocquencourt
BP 105 - 78153 Le Chesnay Cedex
inria.fr

ISSN 0249-6399